## Nanoelectronics and Its New Materials –

# A NEW ERA OF NANOSCIENCE

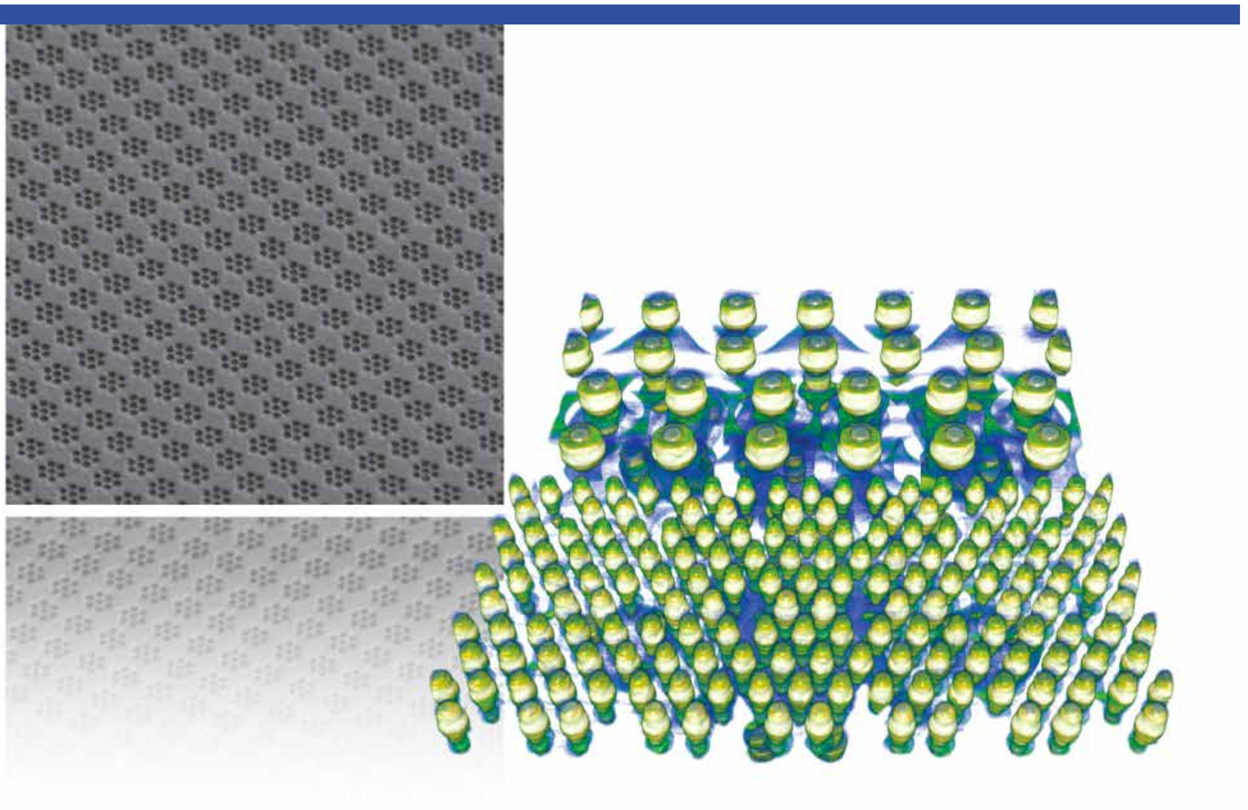

ZEISS

Seeing beyond

WILEY

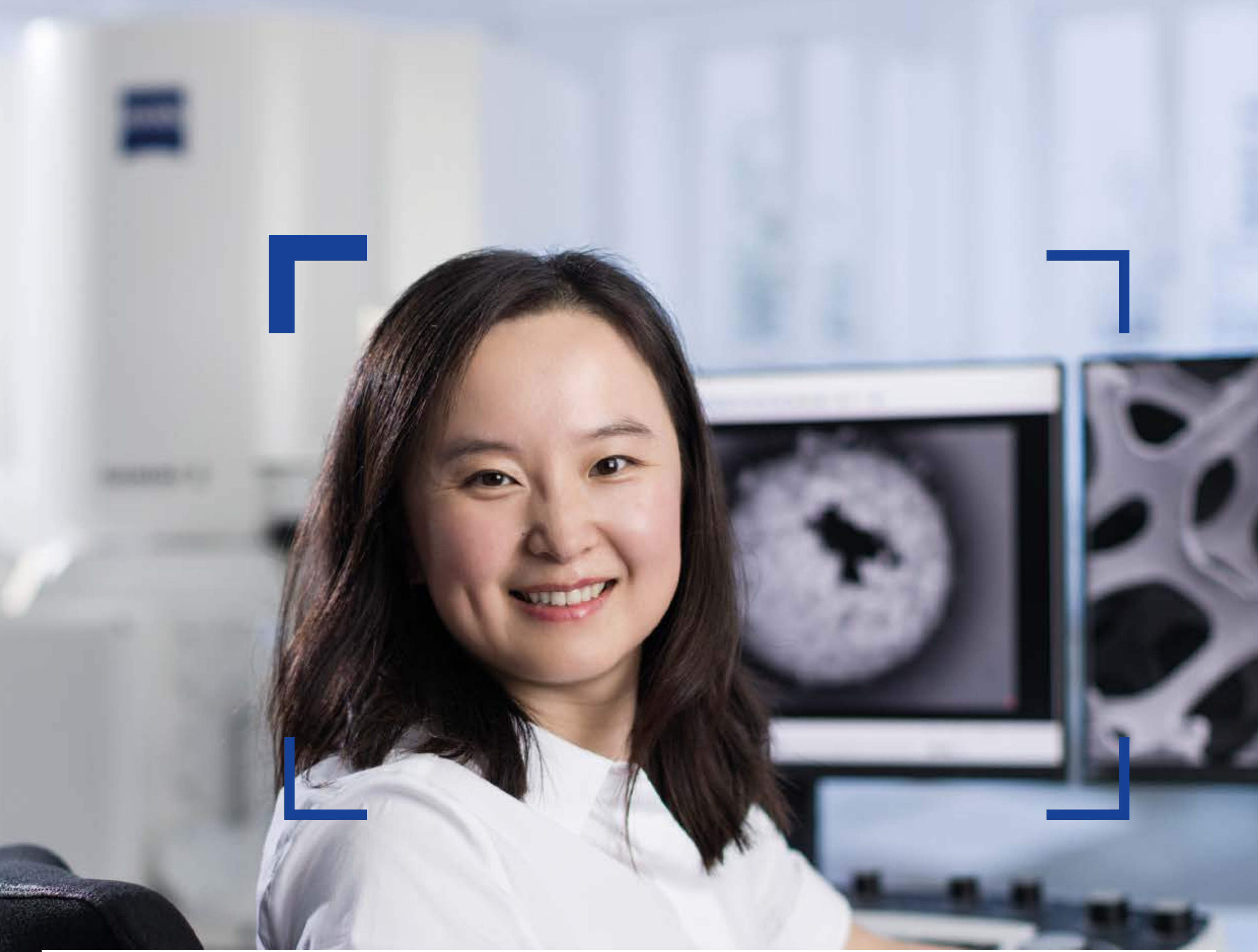

# Editorial

"There is plenty of room at the bottom." With this quote, one could claim that Professor Richard Feynman started the advent of nanotechnology at the American Physical Society meeting at the California Institute of Technology in 1959. Nanoscience or nanotechnology investigates extremely small objects: They are governed by a different set of physical principles compared to ordinary objects in daily life. Nanoscience looks at the effect of these quantum rules on materials whose properties are limited in size, dimension, or both and their interactions with the surrounding environment lead to phenomena that provide unique effects. Thus, nanotechnology methods provide fundamentally new devices and therefore are today's main driving force in areas including electrical and mechanical engineering, materials science, physics, chemistry, and biological sciences. One of the main applications of nanotechnology is in the electronics industry. Many researchers working in scientific and industry development labs expect the pace of computing advancements to go on, enabled by quantum computers, beyond Moore's law. It is assumed one will be able to pack more and more devices onto a computer chip, that the devices will get smaller, faster, consume less power and become cheaper. Overall, very high expectations have been put on the development of new materials needed by nanoelectronics research to continue the pace of Moore's law.

In this compendium, a range of novel applications is presented that describe recent advances in the fields of electronics research and fundamental nanoscience. It is clear that this field has huge potential for expansion and microscopy techniques will continue to be used at the forefront of these advances.

**Dr. Ben Tordoff**
Head of Materials Science
ZEISS Research Microscopy Solutions

**Dr. Olena Vertsanova**
Business Sector Manager, Nanoscience
ZEISS Research Microscopy Solutions

# Contents

## Imprint

Boschstr. 12,
69469 Weinheim, Germany
Email: info@wiley-vch.de
Editors:
Dr. Cecilia Kruszynski &
Róisín Murtagh

# Introduction

The use of new nanomaterials has opened up a new era of nanoelectronics. Introducing integrated electronic circuits (IC) with characteristic topological dimensions of elements smaller than 100 nm based on quantum effects in their nanostructure has been a groundbreaking innovation. Unlike traditional microelectronics, whose processing capability will reach a limit in the next decade, further development of electronics will only be possible based on fundamentally new nanomaterials.

Graphene and similar monolayers are one atom thick materials. They have remarkable properties that can be combined to create various electronic circuits. Carbon nanotubes (CNTs) allow not only for a reduction in the size of transistors but also give electronics truly revolutionary properties, both mechanical and optical. CNTs do not retain light, are mobile, and retain the electronic properties of circuits.

Plasmonics is a further promising field of research in nanoelectronics. Collective oscillations of free electrons inside a metal have a characteristic plasmon resonance. It transpires that it is possible to transmit an electromagnetic wave along a chain of metal nanoparticles and excite plasmon oscillations. Thus, logical chains work much faster and pass on more information than traditional optical systems, and the dimensions of the systems are much smaller than the accepted optical ones.

With the transition to the nanoscale, quantum effects began to dominate in circuits, which opened up many new properties. Accordingly, this signified the prospects for their beneficial use. Furthermore, microelectronic quantum effects often remained parasitic since with a decrease in the size of a transistor, the tunnel effect began to interfere with its operation. The field of nanoelectronics, on the contrary, is designed to use such effects as the basis for heterostructural electronics with a wide range of new research directions.

The development of technology for high-density interconnections of 3D architectures makes failure analysis a necessity. Advanced instrumentation and techniques for imaging and analysis are required here. The most effective method for studying nanostructures is electron microscopy, which

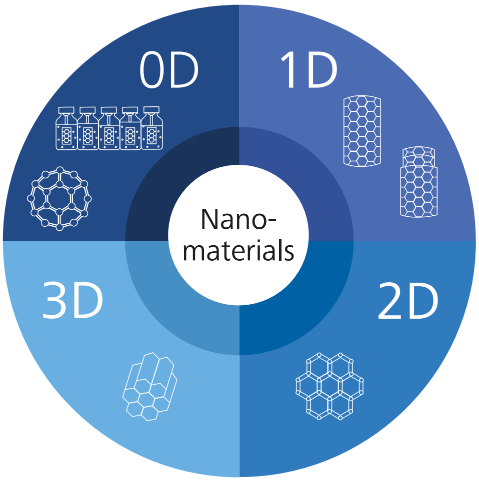

***Figure 1:*** *Overview of nanomaterials as a 4D material parameter space. 0D: quantum dots, fullerenes; 1D: carbon nanotubes, horns; 2D: layers, graphene; 3D: arrays.*

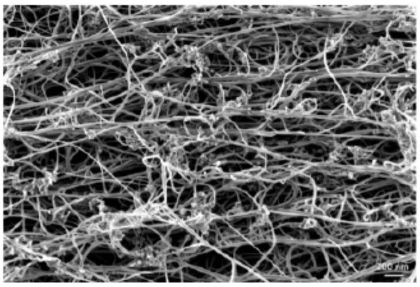

***Figure 2:*** *Carbon nanofibers, SEM image acquired using ZEISS Sigma FE-SEM with the Inlens SE detector at 1 kV in high vacuum.*

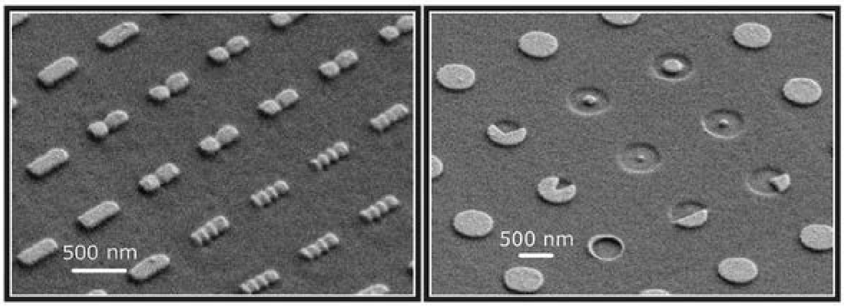

***Figure 3:*** *SEM images of metallic nanostructures fabricated by combining electron and gold ion beam lithography. High-resolution electron beam lithography (IBL) is used to define (left) rod- and (right) disk-shaped gold nanostructures in a lift-off process. In mark-based IBL overlay processes the predefined structures are reshaped by milling parts of the nanostructures by the impinging gold ions. The optical near- and far-field properties can thus be fine-tuned.*

*[Image from [1]]*

makes it possible to visualize the three-dimensional structure of an object with ultra-high resolution and establishes a structure-property relationship, and confirms or refutes the prediction of properties of the nanomaterials. Additionally, data derived from 3D non-destructive X-ray microscopes (XRM) and the correlation of both XRM and EM techniques are vital to put nanoscale details into the context of a larger sample volume.

## Essentials for investigations at the nanoscale

Electron microscopes (EM) equipped with accessories like an energy dispersive spectrometer (EDS), a pattern analysis system for electron backscatter diffraction (EBSD), a cathodoluminescence detector or other analytical attachments, expand the analytical capabilities of microscopy and probe important scientific questions. Typical questions include the investigation of morphological features and elemental composition of materials, individual particle size measurements, phase distribution, and crystalline inclusion analysis.

When operating an FE-SEM (field emission SEM) superior imaging at low kV beam energies is required not only for passive voltage contrast but also for nanoprobing, essential investigation techniques in nanoelectronics. FE-SEMs equipped with ZEISS Gemini electron optics are optimized to meet these challenges. Furthermore, correlative XRM-SEM or focused ion bean scanning electron microscope (XRM-FIB-SEM) workflows steered by dedicated software tools, all from the same source, accelerate the creation of meaningful results by connecting tools seamlessly and enabling researchers to quickly navigate between multiple length scales and imaging modes.

A FIB-SEM with a built-in femtosecond (fs) laser, a LaserFIB, offers quick access to the internal structure of an object, even if it is deeply buried, and gives the ability to prepare, for example, a cross-section for examination. The LaserFIB enables fast defect or package failure analysis and process optimization. It integrates an fs-laser for speed, a gallium beam for accuracy, and an SEM for high-resolution 3D imaging and analysis. The isolated laser chamber prevents contamination of the FIB-SEM's columns and detectors while ensuring sample integrity with easy transfer between the FIB-SEM and laser chamber under vacuum. The sample is protected from oxygen exposure throughout the entire semi-automated preparation sequence and the analysis is accurate. The

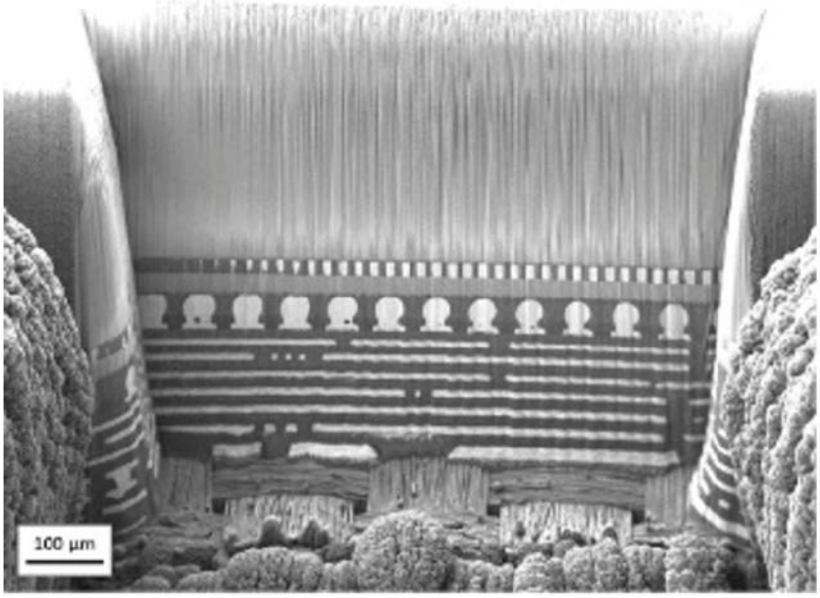

**Figure 4:** *SEM cross-sectional image of a 14 nm silicon node 3D flip chip package immediately after laser polishing, without any ion beam clean-up acquired with a ZEISS FIB-SEM*

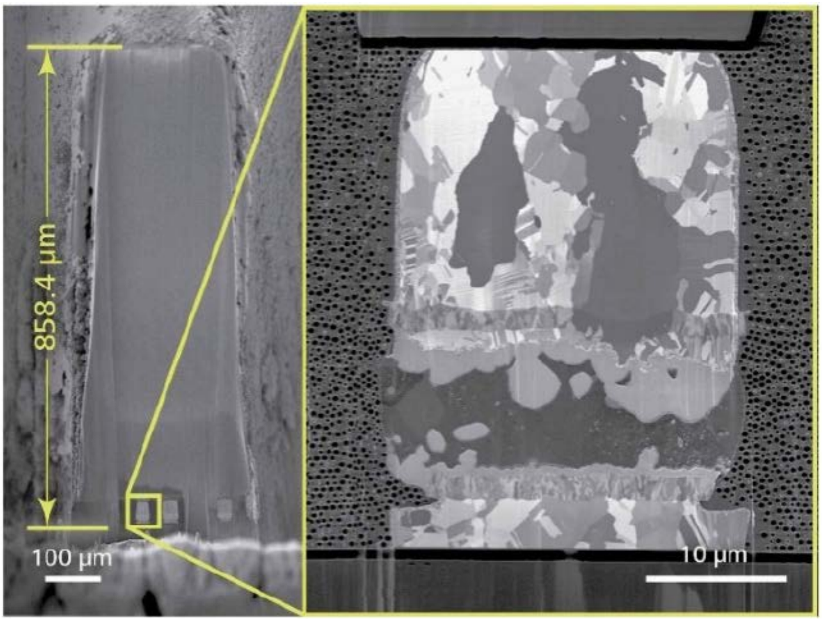

**Figure 5:** *High-quality laser-milled, cross-sections of 25 µm diameter Cu-pillar microbumps and back end of line (BEOL) structures buried 860 µm deep in a 3D integrated circuit package with a total time to results of less than one hour.*
*Left: 3D IC prepared using laser ablation and FIB polishing.*
*Right: Backscattered electron image of a microbump, acquired with ZEISS Crossbeam laser, a LaserFIB.*

fs-laser performs site-specific removal of for example, 1 mm$^3$ of silicon with minimal artifacts in 5 min, compared to the days it would take other commonly used approaches. The laser workflow also avoids mechanical polishing artifacts such as delamination or cracks in fragile and stressed materials, while providing higher cross section accuracy than mechanical cross sections without introducing external stresses. Fs-laser ablation is athermal, so the laser affected zone (LAZ) is minimal, and it is often possible to image package that interconnects immediately after laser ablation without the need for FIB polishing.

Non-destructive 3D X-ray imaging delivers exceptional visualization and structure contrast at the submicron resolution, creating 3D datasets that can be viewed from any orientation using interactive virtual cross-sections. 3D XRM provides scans to accurately localize defects and correlate with a sample preparation technique, such as FIB-SEM. It also delivers a crucial high-resolution look inside the part before any further investigation, including destructive physical analysis. Users obtain data in a matter of hours and virtual 2D cross sections at any location or orientation required. Advanced artificial intelligence (AI)-powered tomography reconstruction techniques are now being used to improve scan throughput by 4x – 10x. 3D XRM is the ideal instrument to visualize buried defects and key structures within intact samples in a non-destructive manner.

## Summary

High-resolution and automation in microscopy as well as correlative workflows between 3D non-destructive X-ray microscopes and SEMs or FIB-SEMs provide new capabilities for semiconductor research, nanofabrication, IC, and failure analysis. Correlated workflows in particular grant access to knowhow in materials research and development of advanced materials for nanoscience and nanoelectronics.

### Reference

[1] Hentschel, M., Karst, J., Giessen, H., Tailored Optical Functionality by Combining Electron-Beam and Focused Gold-Ion Beam Lithography for Solid and Inverse Coupled Plasmonic Nanostructures. Adv. Optical Mater. 2020, 8, 2000879. https://doi.org/10.1002/adom.202000879

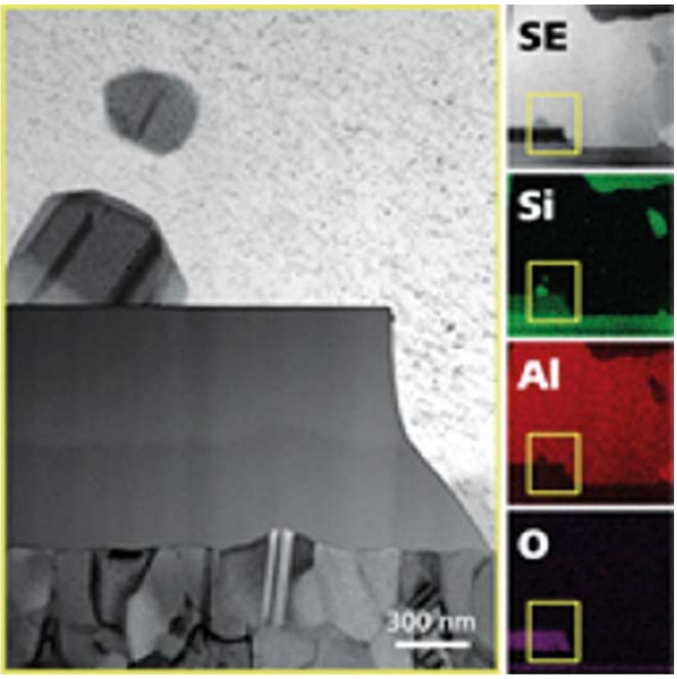

***Figure 6:*** *Cross-section and EDS of insulated gate bipolar transistor (IGBT) examination of the edge of a gate in an IGBT device. Cross section and EDS elemental analysis was performed entirely on a Crossbeam 550 FIB-SEM. Brightfield 30 kV STEM-in-SEM image of lamella combined with EDS elemental mapping in Crossbeam revealed crystalline Si precipitates.*

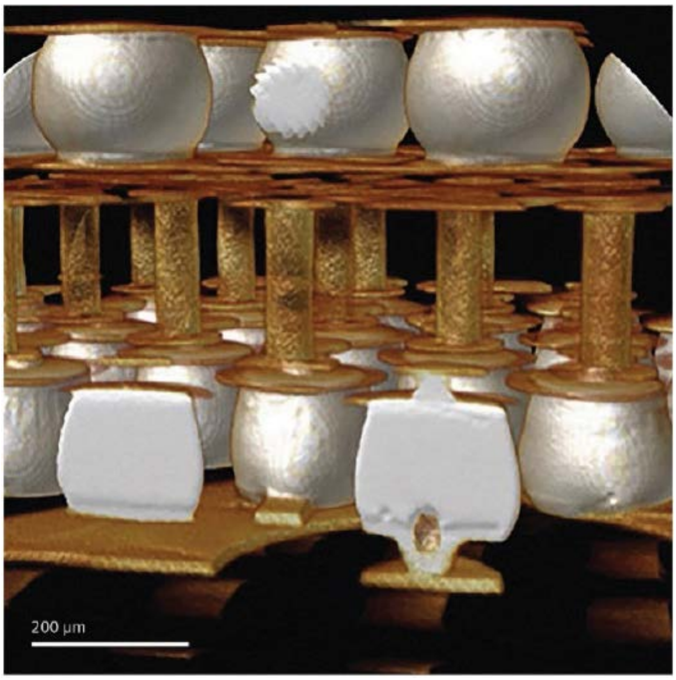

***Figure 7:*** *3D X-ray microscopic images of a package-on-package (PoP) assembly shows the microstructure of the stacked package including top and bottom package bumps affixed to a circuit board. Acquired with ZEISS Xradia Versa.*

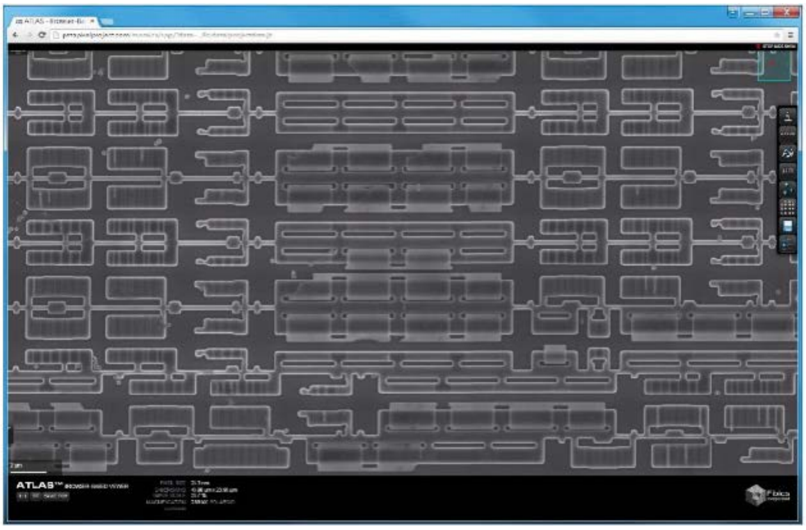

***Figure 8:*** *Deprocessed integrated circuit, acquired in 10 h for a total of more than 90 Gb of image data with Zeiss Atlas 5.*

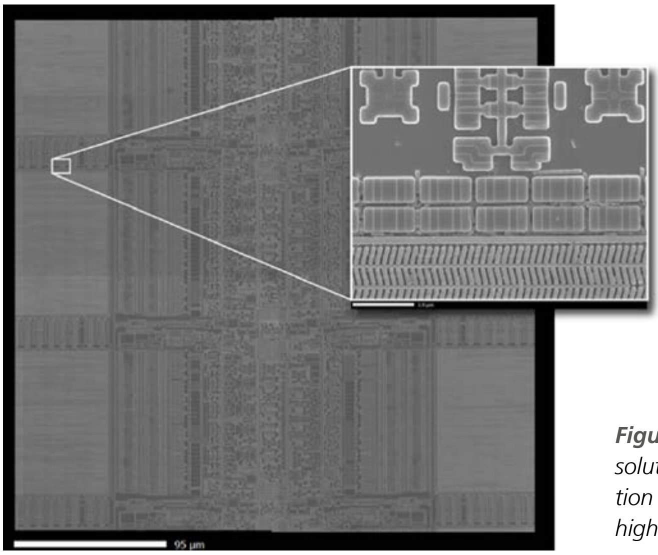

***Figure 9:*** *High-resolution FE-SEM with Atlas 5 – the leading solution for automated, distortion-free, large area tiled inspection of semiconductor die with inset showing structures at high magnification.*

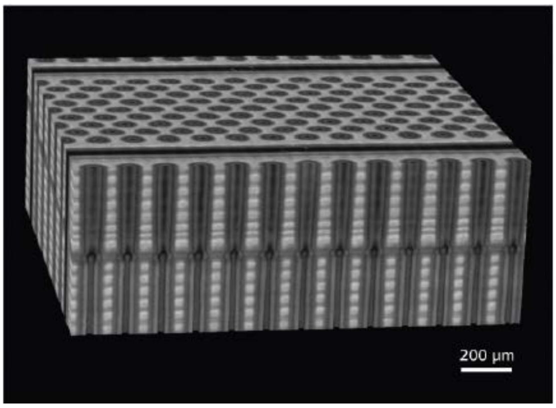

***Figure 10:*** *FIB-SEM tomography of a 3D NAND sample acquired using ZEISS Crossbeam 550 and Atlas-3D. Sample was depackaged and mechanically polished down to the topmost word line. It is shown a virtual is a virtual sub-volume of 2 x 1.5 x 0.7 µm$^3$ size, extracted from the dataset at the transition region of upper to lower deck. Reconstructed voxel size 4 x 4 x 4 nm$^3$. The resulting reconstruction allows for looking at multiple planes of section across the device from any virtual section.*

# High-contrast SEM imaging of supported few-layer graphene for differentiating distinct layers and resolving fine features: There is plenty of room at the bottom

Adapted from Huang, L., et al. 2018

Revealing the structure-property relationships for graphene-based devices requires reliable differentiation and clear visualization of distinct graphene layers and their fine features (e.g., wrinkles). Scanning electron microscopy (SEM) can produce high-quality images, but researchers in the graphene community have overlooked the effect of key parameters on image contrast. Simultaneously tuning acceleration voltage ($V_{acc}$) and working distance (WD) can produce superior secondary electron (SE) image contrast of few-layer graphene supported on silicon carbon (SiC) substrates collected by Everhart-Thornley (E-T) SE detector.

## Introduction

Graphene is often used on a supported platform in electrical devices. Geometrical and structural characteristics such as defects (folds, voids, ruptures, wrinkles), contamination, and dimensions affect performance and its properties. They need to be elucidated and quantified for quality control of fabrication processes. SEM, transmission electron microscopy, Raman microscopy, and atomic force microscopy have been used to characterize the geometrical and structural properties of graphene on substrates. SEM analysis has successfully characterized structures at nanoscale resolution, growth mechanisms, contamination, and the number of layers in supported graphene materials. The SEM with the frequently used secondary electron detector, Everhart-Thornley (E-T) SE detector at low acceleration voltage ($V_{acc} \leq 5$ kV), obtained good image contrast for supported graphene materials. Varying the working distance (WD) can further improve image contrast for supported thin films.

Here, Huang and colleagues systematically tuned the $V_{acc}$ and WD of an SEM to visualize fine features with superior image contrast of graphene (G) transferred to the silicon oxide on a silicon substrate ($SiO_2$/Si) and epitaxial graphene grown on a SiC substrate. The morphologies of G/SiC were characterized by FE-SEM. The FE-SEM system (ZEISS Supra 55 Sapphire) features two secondary electron (SE) detectors.

## Demonstration of superior E-T SE image contrast under combined low $V_{acc}$ and large WD

The SEM images of the same region of a G/SiC sample obtained with the routine $V_{acc}$ (10-20 kV) and WD (8–12 mm) settings were compared to those taken with modified $V_{acc}$ and WD combinations. The SEM images obtained with routine settings did not reveal distinct graphene layers, narrow strips, and wrinkles. Adjusting the brightness/contrast setting improved the contrast number but the image had a grainy appearance and did not resolve the fine details (e.g., narrow strips and wrinkles). In contrast, the SEM images obtained with low $V_{acc}$ (3 kV) and large WD (15 mm) settings showed fine features such as wrinkles and strips in enhanced true image contrast.

## Systematic analysis of E-T SE image contrast under different $V_{acc}$ and WD settings

Figure 1 presents a series of SEM images with an E-T SE detector obtained at the indicated $V_{acc}$ and WD settings. Huang and colleagues used the contrast value CV <0.1 as indicating poor contrast, CV between 0.1 and 0.2 as fair contrast, and CV ≥0.2 as good contrast. Good contrast (green) was obtained with the combination settings of $V_{acc}$ 1 KV/WD 5 mm; $V_{acc}$ 3 KV/WD 15 mm; $V_{acc}$ 5, 10, or 20 KV/WD 20 mm; $V_{acc}$ 10 or 20 KV/WD 30 mm; and $V_{acc}$ 20 KV/WD 40 mm. These results clearly demonstrated that simultaneously tuning $V_{acc}$ and WD can markedly improve image contrast for G/SiC.

## Three types of SE collected by an E-T SE detector

Electron beam interaction with the sample produced SE, backscattered electrons (BSE), and X-rays. The primary electron beam generates type I SE (SE1) with a resolution of 1-2 nm (comparable to the beam's diameter). BSE, which presented energy from 50 eV, was scattered within the near-surface area for tens to hundreds of nanometers and generated Type II SE (SE2). BSE colliding with chamber walls and interior components generated type III SE (SE3) with an escape area similar to SE2. SE3 is a major component of all SE collected by the collector, with estimates of 60-70% for heavy elements and 40-50% for light elements.

## $V_{acc}$ dependence of the SE image contrast for supported graphene

The brightness of a pixel in an image is determined by the total amount of the three types of SE ($N_{1+2+3}$) from the region collected by the E-T SE detector. Image contrast reflected the difference in $N_{1+2+3}$ ($\Delta N_{1+2+3}$) from different regions: larger differences in $N_{1+2+3}$ between regions provided greater image contrast. Thicker or multiple layers of graphene reduced the SE and BSE collected by the detector whereas bare SiC allowed the detection of greater amounts of

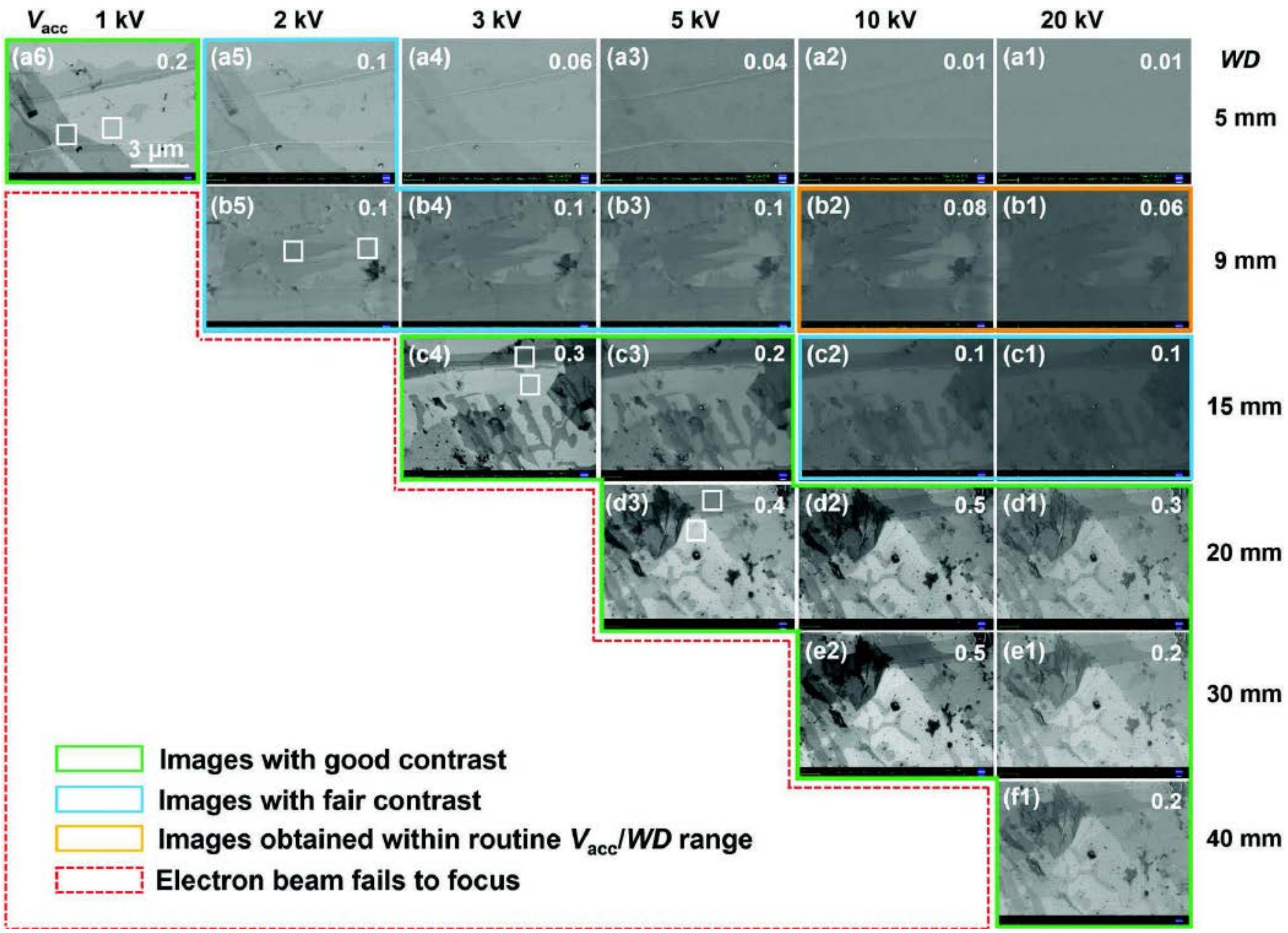

***Figure 1:*** *SEM images for G/SiC were collected with E-T secondary electron detector at the indicated combinations of $V_{acc}$/WD settings. Two regions of bare SiC and double-layer graphene were used to calculate the CV number shown in the upper right corner.*

SE. At lower $V_{acc}$ settings, the incident electrons more efficiently transferred energy to the sample of a material.

### WD dependence of E-T SE image contrast

Increasing WD improved the image contrast because it increased the SE1 and SE2 ($N_{1+2}$), which can overwhelm SE3's negative influence on image quality (Fig. 2). At low WD, the contribution of SE3 to the total SE is greater than at high WD (Fig. 2a). SEM images with the E-T SE detector showed improved image contrast with increasing WD and constant $V_{acc}$ (Fig. 2c). Figure 2b illustrates that the E-T SE detector captured more SE1+2 at large WD than at small WD. The detector also captured less energy from SE3 ($N_3$) at a large WD.

### Benefits and limitations of combined tuning of $V_{acc}$ and WD for high-contrast imaging of supported graphene

The contrast in SEM images markedly improved by using low $V_{acc}$ and large WD settings on the E-T SE detector. This strategy has been overlooked by many researchers studying graphene characteristics on various substrates. One limitation of using small $V_{acc}$ and large WD settings may be decreased spatial resolution. Its effect on the spatial resolution may be minimal at magnifications ≤50,000 but may become a limitation at magnifications ≥100,000. The benefits of the combined tuning may also be dependent on the type of substrate as electron-induced charging may occur on the edge contrasts on insulating substrates $SiO_2$.

### Conclusions

Tuning $V_{acc}$ and WD of the SEM E-T SE detector markedly improved SEM image contrast for $G/SiO_2/Si$ and G/SiC. Huang and colleagues presented a model suggesting that $V_{acc}$ and WD influence the quantity of the three types of SE collected by the E-T SE detector. When the SEM E-T SE detector settings include lower $V_{acc}$ and/or larger WD, the improved image contrast is due to the increasing difference in total SE collected by the detector. These results suggest that these settings may improve effective characterization of other thick 2D materials and devices.

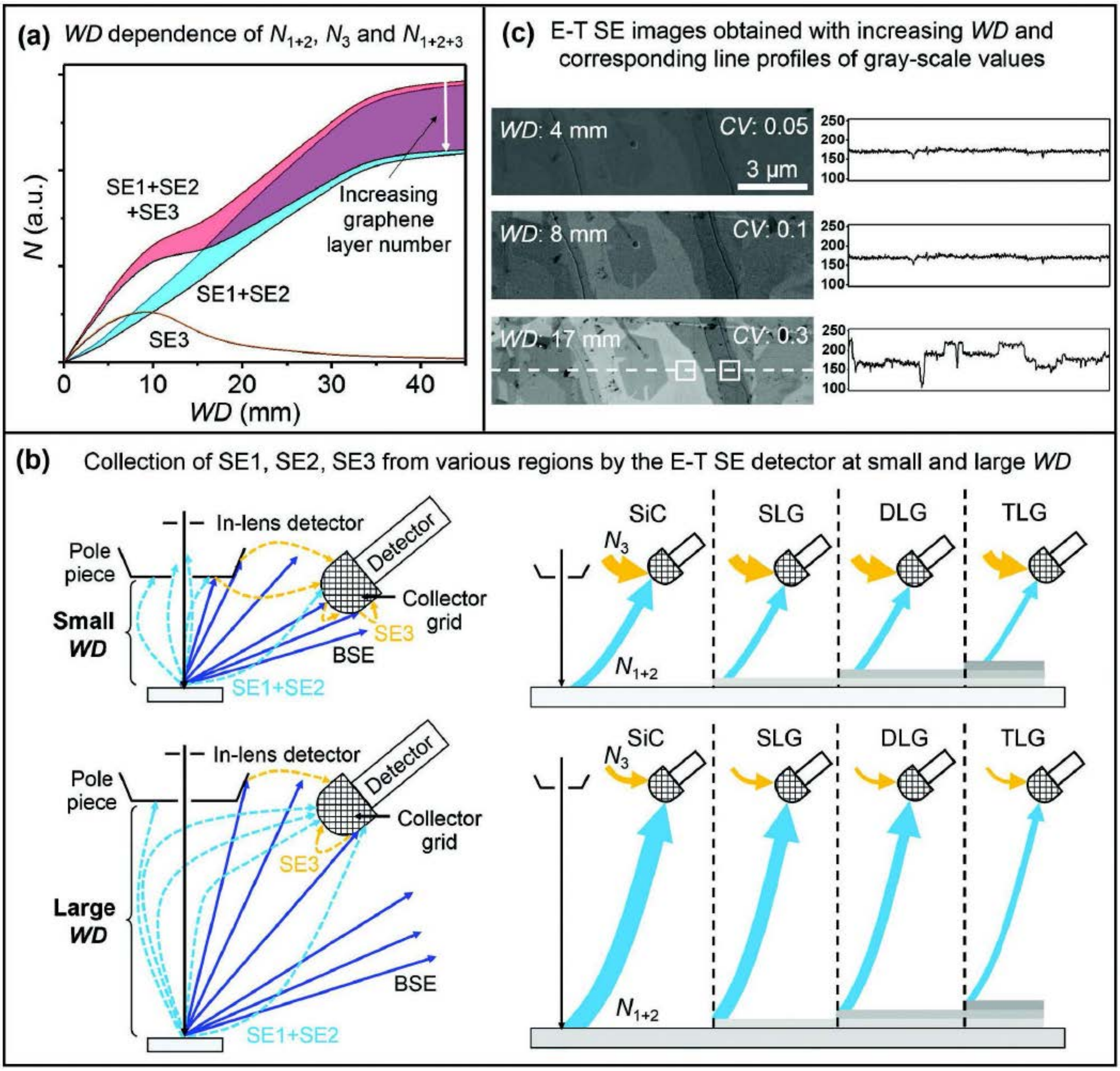

*Figure 2:* *Effect of increasing WD on measuring the three types of SE by an E-T SE detector. (a) Schematic plot of energy from SE1+2, SE3 as a function of WD. (b) Schematic of the effect of WD on collection performance of the E-T SE detector and $N_{1+2}$, $N_3$ from various regions of bare SiC or SiC with single (SLG), dual (DLG), or triple (TLG) layer of graphene. Arrow thickness represents the quantity of SE entering the detector. (c) SEM images of G/SiC were obtained at $V_{acc}$ at 3 kV and WD at 4, 8, and 17 mm. Line profiles represent the corresponding grayscale values of the adjacent SEM image.*

# Lithium detection with secondary ion mass spectrometry correlation of surface topography and chemical analysis

Adapted from Wilhelm, G. et al. 2022

Secondary Ion Mass Spectroscopy (SIMS) is efficient in detecting lithium, a major component of batteries used in many electric vehicles. The process of aging in batteries has not yet been elucidated in detail. Analyses with SIMS equipped with three different detectors including an Electron Dispersive Spectroscopy detector provided new insights into the aging process of lithium-ion batteries. The combination of secondary electron images and element mappings allowed the correlation of surface topography, including the identification of micro- and nanostructures on the lithium anode, with chemical analysis. Chemical compounds were identified by comparing the mass spectra of standard samples with the spectra from aged anodes.

## Introduction

Electric vehicles require batteries with a long lifetime and high performance. Lithium-ion batteries are often used in electric vehicles, and their aging involves lithium deposition on the anode surface, which decreases the capacity of the battery. However, little is known about the aging process of the structures and the changing chemical composition of the batteries. Imaging with SIMS, secondary electrons, and correlative visualization of lithium were employed to characterize the anode in aged li-ion batteries.

## Experimental methods

Three different reduced capacity (<80%) nickel-manganese-cobalt oxide (NMC)/graphite battery systems that had undergone >900 charge and discharge cycles were investigated with the following equipment. First, a ZEISS crossbeam 540 focused ion beam scanning electron microscope was equipped with a Gemini II column, an Inlens detector, a Schottky field emission electron gun, and an Oxford Ultim Extreme Electron Dispersive Spectroscopy (EDS) detector. Gallium ions were used in the focused ion beam. Second, SIMS used a Hiden quadrupole detector and ZEISS time of flight detector for SIMS analysis. Third, a ZEISS Orion NanoFab focused ion beam system was used with a magnetic sector detector that worked with helium or neon ions.

## Visualization of surface topography

Secondary electrons detected with scanning electron microscopy revealed that the anode graphite plates are covered with three types of structures. The encrustations were a few nanometers thick (Fig. 1a). The nanoparticles ranged from approx. 10 nm to 100 nm in diameter (Fig. 1b). Large precipitates including fibers were in the micrometer size whereas spherical particles span about 100 to 500 nm (Fig. 1c) or larger. The three types of particles were distributed unevenly along the anode. Electron Dispersive Spectroscopy (EDS) analysis revealed carbon as the most abundant element. EDS analysis also indicated that oxygen and fluorine were more abundant in the anode-cycled field spectrum than in the anode-cycled point spectrum. The presence of small amounts of sodium and phosphorous was detected in the anode-cycled field spectrum (Fig. 1d). Phase mapping indicated that the measuring point of the EDS point spectrum was in a region with low oxygen and fluorine; both elements were associated with nanoparticles.

## Chemical composition of structures

A high lithium signal allows its mapping using SIMS and imaging of secondary electrons. High oxygen concentration improved lithium detection. Lithium was found on the full anode surface of cycled batteries, including all structures (e.g., encrustations, spherical nanoparticles, and large particulates). SIMS detected *m/z* 33 signals in the large fibers in the cycled anode which can be interpreted as the positive ions, $Li_2F^+$, $Li_2Li_3^+$, and/or $OLi_2^+$. Comparison of the spectrum of standard samples for these positive ions would provide further insights into the composition of large fibers. SIMS also detected *m/z* 55 enriched in small fibers. The result *m/z* 55 can be interpreted as manganese, which suggests the decomposition of the cathode material. The cathode contained the elements manganese, cobalt, copper, and nickel.

In comparison to conventional SIMS, the ZEISS Orion NanoFab can provide a higher lateral resolution, distinguishing between spherical particles and nanoparticles (Fig. 2a). Spherical particles exhibited a high signal for lithium *m/z* 6 (Fig. 2b), fluorine *m/z* 19 (Fig. 2c), and oxygen *m/z* 28 (Fig. 2e). Nanoparticles contain not only those traces but also silicon (Fig. 2d). Semi-quantitative analysis of the mass spectroscopy results provided further insights into the composition of the spherical particles, nanoparticles, and separators on the cycled anodes (Fig. 2, bottom histograms).

SIMS can also detect and resolve peaks of single isotopes and molecules. Comparison of the mass spectrum of a lithium fluoride molecule and the mass spectrum of the cycled anode indicated the presence of LiF precipitated on top of the cycled anodes. It also detected the presence of LiF in large

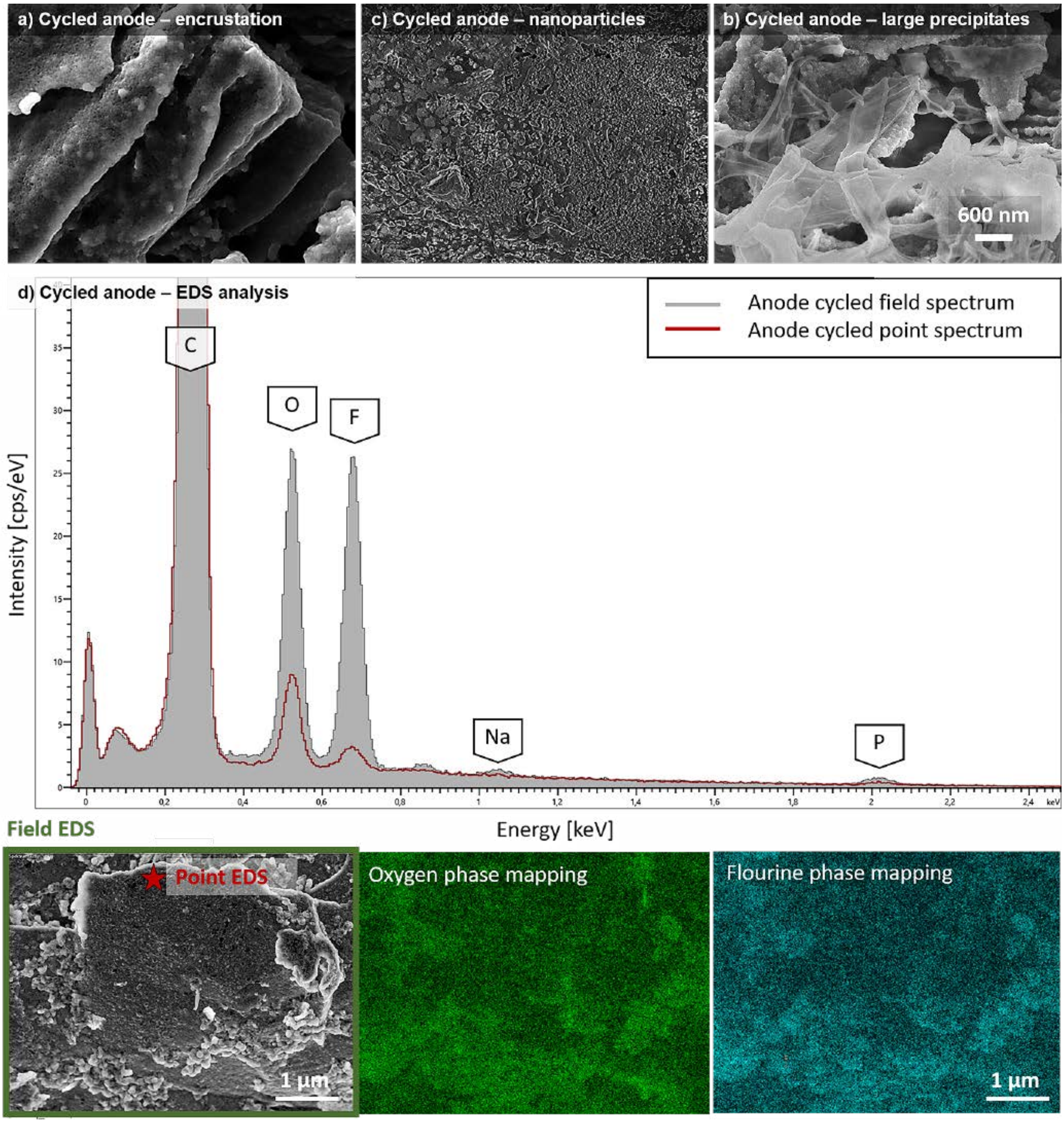

***Figure 1:*** *High lateral resolution of surface topography of lithium battery anode. Graphite plates are covered in uneven distribution with (a) encrustation, (b) nanoparticles/small grains, and (c) large particulates including fibers and spherical particles. (d) EDS analysis of cycled anode surface by cycled point analysis and cycled field analysis. Note the differences in oxygen, fluorine, and phosphorous content between point and field analysis.*

fibers. Since *m/z* 33 in large fibers can be interpreted as the positive ions, $Li_2F^+$, $Li_2Li_3^+$, and/or $OLi_2^+$, additional standard sample measurements are needed to provide a correct interpretation of *m/z* 33. SIMS analysis of the lithium content reveals the presence of lithium in all structures. Nanoparticles have lithium bound with oxygen, fluorine, and/or silicon. Lithium is bound to fluorine and oxygen in spherical particles. Both lithium and manganese are found in small fibers. Mass spectroscopy of standard samples of specific molecules such as LiF can be used as a fingerprinting technique and can enhance the interpretation of the SIMS results.

## Conclusions

Aged batteries, particularly aged anodes, show a surface topography with encrustation, nanoparticles, and large precipitates by secondary electron images analyzed with EDS and SIMS. SIMS analysis of the lithium content reveals the presence of lithium in all structures. The analysis of standard samples of potential compounds found in the structures such as LiF enables the interpretation of mass spectra and identification of the exact chemical compounds.

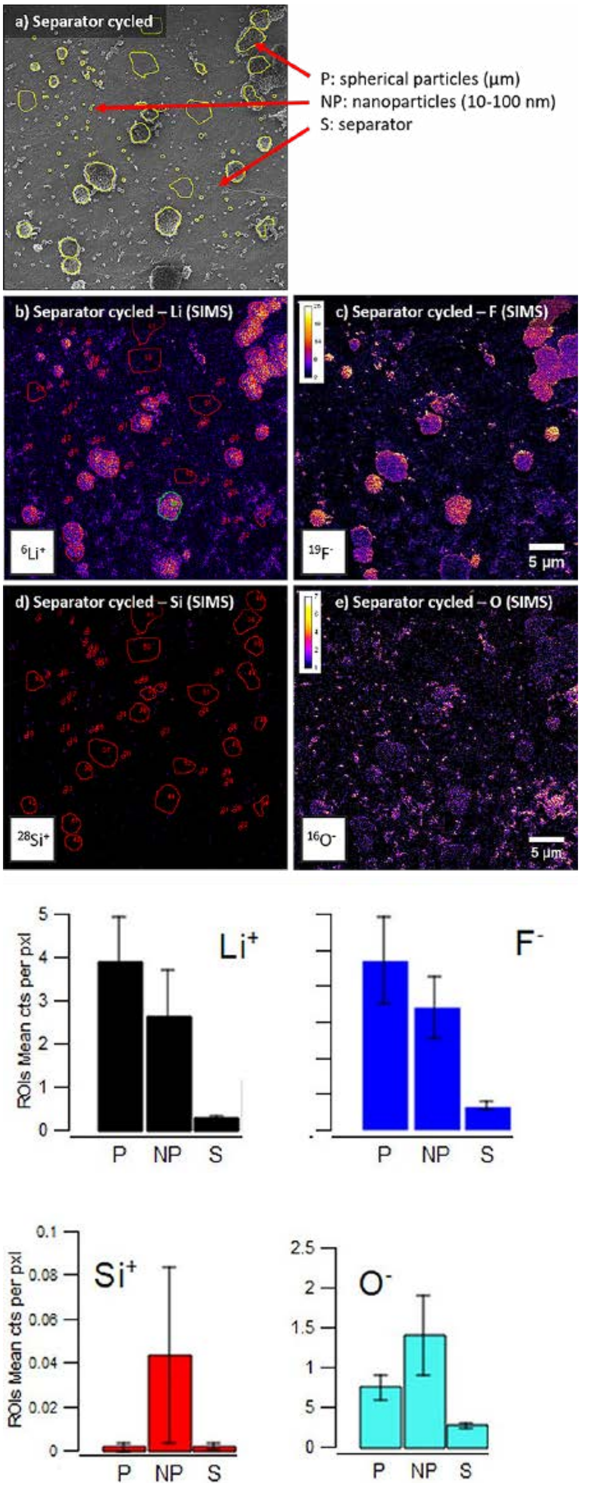

***Figure 2:*** *Surface topography of an anode side of cycled separator foil by the ZEISS Orion NanoFab was correlated with SIMS mapping. (a) High-resolution lateral view showing nanoparticles and spherical particles; visualization of signals for (b) lithium (Li); (c) fluorine (F), (d) silicon (Si); and (e) oxygen (O) on the visualized structures. Bottom histograms provide a semiquantitative interpretation of the mass spectroscopy results of the four elements in the spherical particles (P), nanoparticles (NP), and separators (S).*

# Tailored optical functionality by combining electron-beam and focused gold ion-beam lithography for solid and inverse coupled plasmonic nanostructures

Adapted from Hentschel, M., et al. 2022

Advances in plasmonics usually occur in parallel with progress in the fabrication of micro- and nanonetworks. Significant challenges occur in the fabrication of the plasmonic components. Here, a highly versatile route for the fabrication of high-fidelity and complex plasmonic nanostructures combines gold ion-beam and electron-beam lithography. Both planar and 3D nanostructures demonstrate excellent quality in alignment precision and shape fidelity, with little to no defects. The two complementary techniques were instrumental in fabricating complex plasmonic structures with superior optical functionalities and ultra-distinct spectra features.

## Introduction

Plasmonics is the study of density waves of electrons (plasmons) generated when optical light strikes a metal surface under precise conditions. These plasmons occur rapidly, are very small, and theoretically can encode more information than possible for conventional electronics. However, the development of plasmonic structures is challenging due to their complexity, small sizes, 3D arrangements, structural composition, material composition, and need for shape accuracy. Sophisticated DNA nanotechnology combined with other techniques offers one set of approaches. Alternatively, optical lithography and electron-beam lithography (EBL) can fabricate solid particles of most dielectric compounds or metals into the required well-defined periodic and/or 3D arrangements. However, varying shapes, thicknesses, and complex 3D structures as well as an intrinsically unstable and difficult-to-control fabrication process pose limitations to the use of EBL. Focused ion-beam and transmission electron microscopy membranes also have limitations.

Here, Hentschel and colleagues describe a combined fabrication process involving EBL, gold ion-beam lithography ($Au^+$ IBL) with dedicated eLine and ionLine Plus lithography tools, which have improved focusability and a laser interferometric sample stage. Since gold structures are commonly used in plasmonics, the use of $Au^+$ ions on the $Au^+$ platform reduces contamination with other ions.

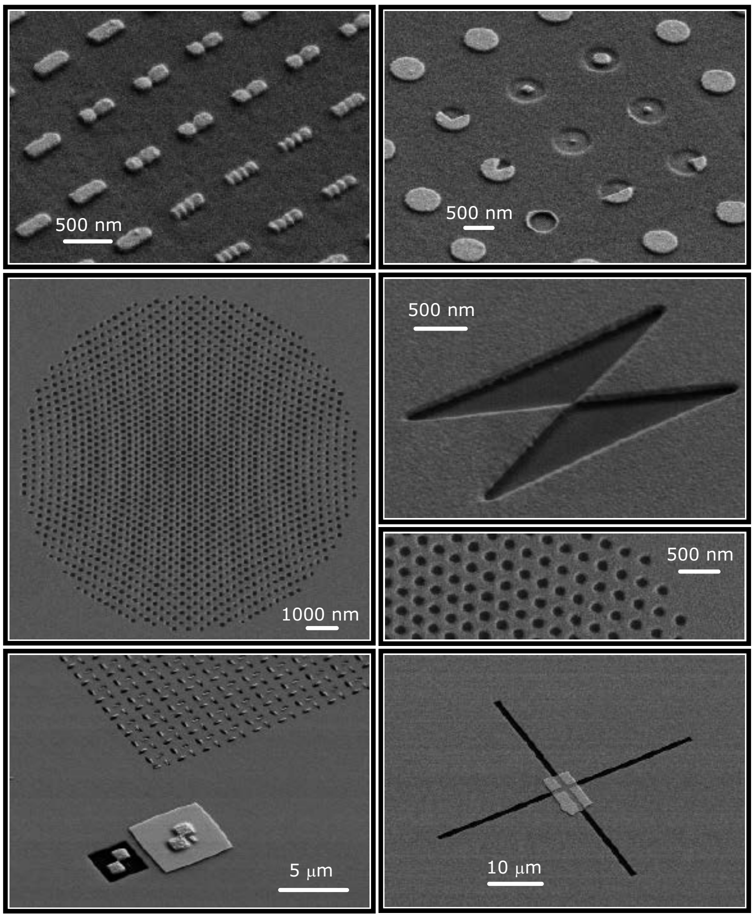

***Figure 1:*** *SEM images of six nanostructures fabricated by EBL, IBL, or their combination. Top row: nanostructures fabricated by EBL and some trimmed by IBL. Second row: inverse nanostructures fabricated by IBL. Third row: alignment marks structured by IBL with EBL-fabricated nanostructures, used for alignment.*

### Complementary properties of EBL and Au$^+$ ion-beam lithography for nanostructuring

EBL and Au$^+$ ion-beam lithography (Au$^+$ IBL) provided complementary properties needed to achieve the fabrication of advanced plasmonic nanostructures. The technique best suited to perform the fabrication step was used. IBL can specify the deposited dose, which determined the milling depth and supported the milling of 3D structures. EBL was used to fabricate solid rod plasmonic structures, which are recognition marks that aligned the two techniques, and Au$^+$ IBL mills the inverse structure.

### Scanning electron microscope (SEM) images of different Au nanostructures

SEM images showed that IBL presented high-resolution capabilities (e.g., 15 nm). Several recognition marks were placed on the structures to align the different steps in the fabrication process. EBL was used both before and after Au$^+$ IBL fabrication steps to achieve the desired 3D nanostructures. Figure 1 shows SEM images of six nanostructures fabricated using EBL, IBL, or a combination of both. EBL fabricated the nanorods and nano-discs in the top row, and some were subsequently trimmed with IBL (top row). The second row showed an Au film structured by IBL as an array of inverse circles (overview and closeup) or a bowtie. The third row showed inter writefield alignment marks fabricated using IBL in an Au film for aligning the second layer of EBL nanostructures.

### Planar plasmonic analog of electromagnetically induced transparency (EIT)

One type of planar plasmonic analog had a single nanorod in near-field coupled to a plasmonic mode. It comprised an out-of-phase oscillation in a pair of parallel rods with dipolar modes (Fig. 2).
An indentation inverse planar plasmonic analog presented a single nanoslit and a pair of nanoslits, which caused the bright and dark modes, respectively (Fig. 2).

Babinet's principle indicates that the roles of reflection, transmission, and polarity directions are reversed in the inverse planar plasmonic analog. The main challenges to the fabrication of planar plasmonic analogs include good shape reliability and a small ridge width to allow efficient coupling and minimize undesired milling of adjacent ridges. The fabrication of inverse solid plasmonic structures can use EBL for the placement of the solid rod and Au$^+$ IBL for the coupling of the dipolar plasmonic mode. The SEM images in the normal and tilted views indicated the overlay accuracy and homogeneity of the fabricated solid-inverse plasmonic structures. Both accuracy and homogeneity are essential for observing sharp features in the optical spectrum.

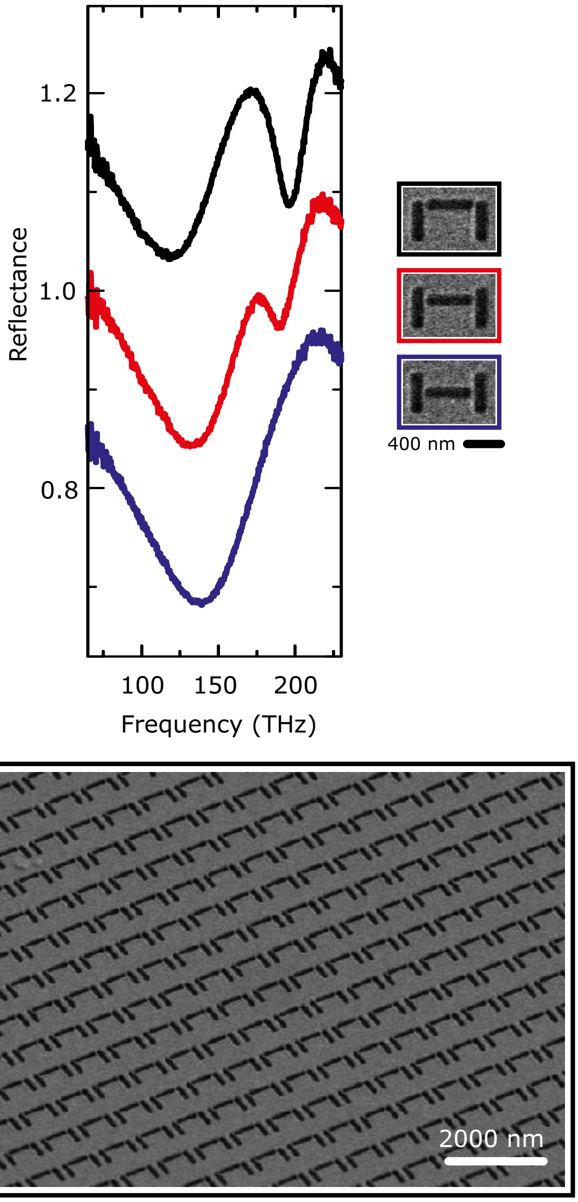

***Figure 2:*** *Spectral profiles and SEM images of the planar plasmonic analog of electronically induced transparency. Top half: Increasing the structure's asymmetry by moving the horizontal nanoslit induces a dark mode comprised of out-of-phase oscillation of the two dipolar modes supported by the pair of parallel slits. The spectra are shifted upward by 0.2 for clarity. Bottom half: Overview SEM image of the strongest coupling structure revealed excellent quality in large-area fabrication. Film thickness is 40 nm Au. Dipole slit is 400 nm x 70 nm, quadrupole wires 360 nm x 70 nm, ridge width 20 nm, periodicity 800 nm in both directions.*

### Coupling phenomena

Complex plasmonics often involves coupling phenomena to produce plasmonic oligomers.

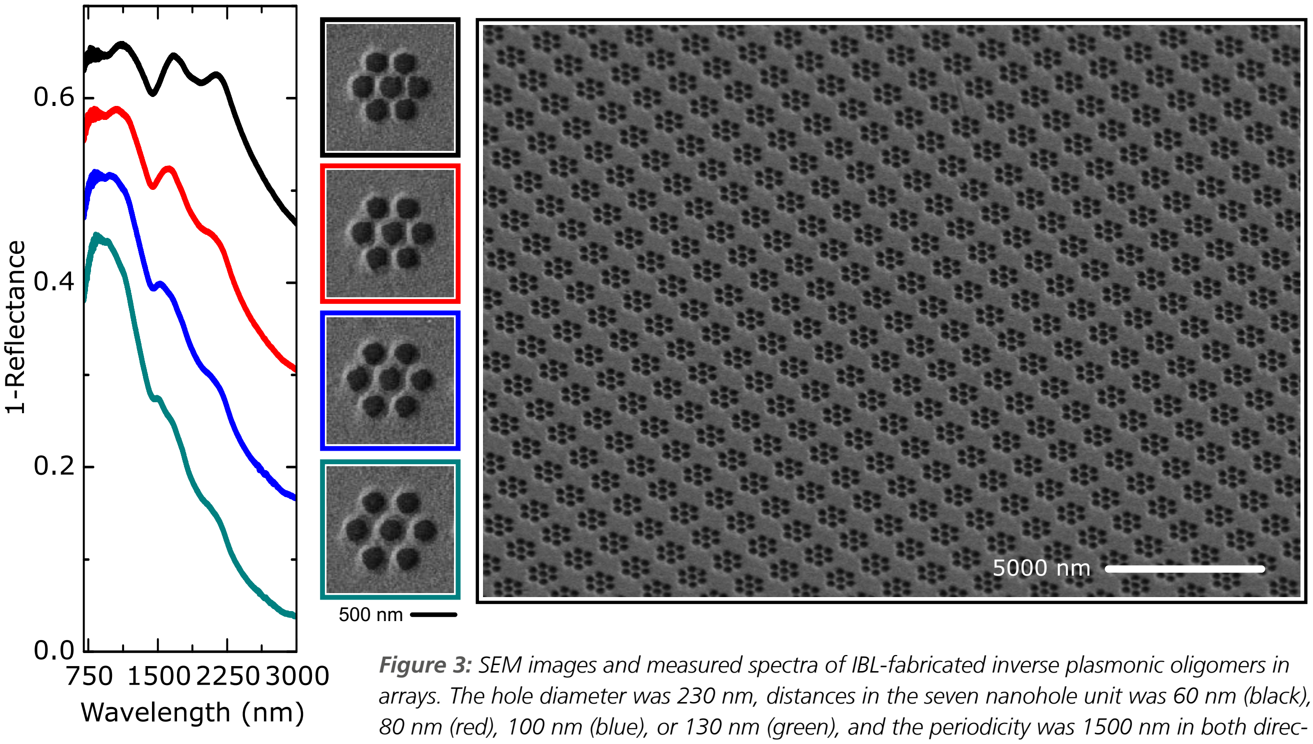

*Figure 3: SEM images and measured spectra of IBL-fabricated inverse plasmonic oligomers in arrays. The hole diameter was 230 nm, distances in the seven nanohole unit was 60 nm (black), 80 nm (red), 100 nm (blue), or 130 nm (green), and the periodicity was 1500 nm in both directions. The spectral profile changed with the reduction in interparticle distance. The spectra were shifted upward by 0.1 for clarity.*

An example is densely packed hexagonal arranged individual disks (Fig. 3). When the distance between disks was small enough, the modes couple and form molecular orbitals or collective modes, which exhibit different properties (Fig. 3).

In quality control, SEM images could document the quality or homogeneity over a 100 µm x 100 µm array (Fig. 3). Spectra also indicated the efficiency of coupling and the homogeneity of the array.

### Infrared resonant nanoantenna arrays and gap antennas

EBL was used to fabricate arrays of infrared resonant nanoantennas. After aligning the $Au^+$ IBL with mark recognition, $Au^+$ IBL, which could modulate deposited dose and milling depth, was used to successively cut the individual antennas to yield a gap antenna.

### Plasmonic chirality

Optical chirality indicates a different response to circularly polarized light from the left (LCP) and the right (RCP) directions. After RCP or LCP excitation, the two chiral nanostructures exhibited significantly different mode signatures in the spectra. The strength of the chiral signal was dependent on the level of structural asymmetry.

### Electric and magnetic distributions from the mixed solid-inverse structure under right circularized polarized (RCP) light

The electric field distributions showed the dipolar pattern associated with the solid rods' fundamental mode, which was characterized by an electric dipole moment. The dipole moments in the magnetic field distributions were associated with the fundamental mode of the slits. The higher energy mode at 2,140 nm was characterized by an in-phase combination of electric and magnetic dipole moments. The lower energy mode at 2,540 nm represented the out-of-phase combination of the electric and magnetic dipole moments.

### Conclusions

These new fabrication strategies combine electron-beam and gold ion-beam lithography in various arrangements to produce complex plasmonic nanostructures, including single-layered nanostructures, gap antennas, plasmonic oligomers that exhibit coupling phenomena, 3D plasmonic nanostructures, optical chiral sensory nanostructures, and mixed solid-inverse plasmonic nanostructures. The plasmonic structures showed excellent accuracy, shape fidelity, and resolution. The combination of EBL and $Au^+$ IBL fabrication techniques appears directly applicable to the fields of plasmonics, plasmonic sensing, and nanooptics.

# X-ray microscopy and automatic detection of defects through silicon vias in three-dimensional integrated circuits

Adapted from Wolz, B. C., et al. 2022

TSVs play a crucial role in connecting and achieving intricate three-dimensional integrated circuit (3D-IC) components, serving as an essential technology. X-ray microscopy (XRM) is a rising method of analyzing the internal structure of bulk samples and may be useful in quality control including failure analysis. This research developed and combined XRM scanning recipes with deep learning object detection workflow to automatically identify the location of defects in Cu liner-TSVs without destructive testing.

## 3D-IC and TSVs technology

Three-dimensional integrated circuits (3D-IC) contain multiple TSVs on a single microchip. TSVs consist of a silicon (Si) wafer embedded in a metal (usually copper (Cu)) isolated by a dielectric intermedium layer. Annealing procedures during the fabrication process can induce thermal stress on the final TSV structure which can lead to structural failures like Si cracking, degradation of Cu liner, and wall delamination.

## Failure analysis methodologies of TSVs

3D X-ray microscopy (XRM) is a versatile imaging technique that can provide internal analysis of certain structures. XRM applies an X-ray beam onto the sample and uses optical and geometric magnification to enlarge the projection and detect the weakened transmitted photons. Advantages of XRM analysis include minimal or no sample preparation (e.g., no mechanical grinding,  embedding, nor polishing), improved spatial resolution, high-resolution imaging of large samples and internal structures, production of the 3D dataset for generating virtual cross-sections or a complete 3D reconstructed image with respective software, and relatively rapid analysis that supports sufficient sample sizes to reach adequate statistical power. Automated machine deep learning strategies are well suited for the simultaneous analysis of many TSVs and the identification of defects in specific TSVs. This study used RetinaNet software for deep learning strategies due to its suitability for microscopy image analysis, performance in class imbalance conditions, good ratio of precision to speed, and large volumetric XRM datasets.

## Current state of research for XRM and deep learning-based TSV analysis

Most current approaches focus on defect localization in high aspect ratio fulfilled TSVs. No studies investigated the automatic detection of delamination defects in liner TSVs.

This study investigated an automated object recognition solution for automatic failure analysis targeting wall delamination defects. The XRM workflow was designed to initially detect large delamination defects in Cu liner TSVs with low-resolution XRM scans followed by high-resolution scans that locate the defects at the micrometer to submicrometer range.

## Scan parameter finding process

All XRM measurements of the application-specific integrated circuits (ASICs) containing low aspect ratio via-last Cu liner TSVs were performed on a ZEISS Xradia Versa 620. The ZEISS Scout and Scan Reconstructor were used for the manual reconstruction of the datasets by applying ZEISS standard corrections for beam hardening and center shift.

An XRM scan of a single TSV on top of an ASIC used scan settings that included a 20x objective, 140 kV voltage, 21 W source power, high energy X-ray filter, 30 s exposure, 184° rotation, 2,401 projections, a detector pixel binning value of 2, and a voxel size of 0.95 µm (Fig. 1).

Wolz and colleagues systematically varied the positioning of the ASIC chip, range of magnification, voltage of the X-ray tube, optimal focus parameters, and exposure values (0.05–30 s) to optimize the full ASIC device scan. Fiji was used to analyze the raw projection images and determine the contrast-to-noise ratio.

## Development of a full device scan recipe

Four different tomography scans that differ in projection numbers (1,601 or 901), detector pixel binning values (1 or 2), exposure time (1 or 8 s), or multiples of variable exposure time (1x or 5x) were performed on a specific ASIC with 3 W power and 40 kV beam voltage, no X-ray filter, 226° rotation, overall magnification of 1.8, and the high aspect ratio tomography (HART) function. Higher voltages and additional filters did not minimize metal artifacts. A measurement time of 5 h was considered a reasonable time for batch standard IC checkup. After consideration of detailed line profile analyses and elapsed times, the chosen optimal recipe for a full device scan on the ZEISS XRM was 0.4× scintillator-coupled objective, 40 kV beam voltage, 3 W power, no X-ray filter, 226° rotation, use of HART function, binning of 1, 1,601 projections, and an 8 s exposure time.

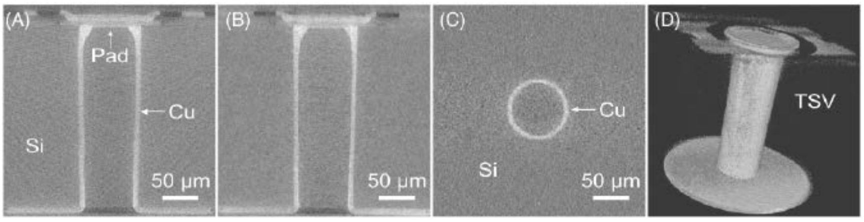

***Figure 1:*** *Three different cross-sectional views of an XRM scan of a single intact TSV on an ASIC and a single 3D illustrated view. (A, B) Orthogonal vertical cross-sections in XZ and YZ; (C) horizontal cross-section in XY at center height; (D) Illustration of the Cu liner, associated metallic components of TSV. Bright areas correspond to the Cu liner and the TSV top pad, which block X-rays more efficiently than Si. The Si and oxide layer are quasi-transparent to X-rays and appear as noise.*

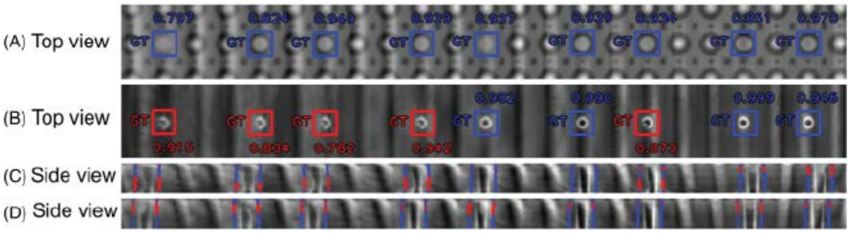

***Figure 2:*** *Predictions from the top view (A, B) and side view (C, D). (A, B) Objects found at differing depths. The confidence score is shown below the bounding box. (C, D) Side-view perspective informs on the depth of the defect and thus TSVs with defects.*

***Table 1:*** *Data distribution for the number of ASICs, analyzed TSVs, and defect and intact TSV slices.*

| ASICs | TSVs | Defect TSV slices | Intact TSV slices | Image resolution | Bounding box size |
|---|---|---|---|---|---|
| 12 | 876 | 8,946 | 20,838 | 1,440 x 1,120 px | 25 x 25 px |

## Development of a detailed TSV scan recipe

Wolz and colleagues investigated multiple parameters for XRM with a 20x objective, an overall magnification of 56×, a binning value of 4, a voxel size of 0.95 µm, an exposure time of 15 s, 2,401 projections, and 184° rotation. The 140 kV, 21 W power scan provides sharper structures at the TSV wall and pad in unsliced TSV than the 40 kV scan. The chosen detailed TSV scan used 140 kV, 21 W power, and a variable exposure time factor of 4 at long view angles and the aforementioned parameters because it yielded the most detail in unsliced TSVs.

## Summary of XRM recipes and suggested analysis workflow

The two recipes for XRM workflow for the detection of integrity or delamination defects in TSVs were (i) a device scan recipe (40 kV) and (ii) a detailed TSV scan (140 kV).

Deep learning was conducted on a reconstructed volumetric dataset. The network is trained and optimized with additional datasets. The development of an automated defect detection system begins with a dataset annotated for TSVs with integrity or delamination defects by an expert. The database in the open-source software EXACT indicated that approximately 30% of TSV slices contain a defect (Table 1).

## RetinaNet

The object recognition software RetinaNet mimics expert performance by detecting and classifying defective or intact TSVs while using scores to assess their reliability. Its ResNet backbone and feature pyramid network (FPN) integrate multiscale features from both the full device scan and the detailed scan of TSVs. Each FPN layer predicted the probability of the presence of delamination or integrity and its classification while the regression network determined its coordinates.

## Object detection results

The object detection software yielded a mean average precision of 0.94 ± 0.01, an average precision of intact versus defect of 0.92 ± 0.04, and an average recall intact/defect of 0.99 ± 0.02. Most misclassifications of the software occurred in the lid region, where experts also had lower accuracy than in other regions. The classification is easier to distinguish from the top view of TSVs (Figs. 2A, B). The classification results from the side view of TSVs can indicate the depth of the defects (Figs. 2C, D).

## Conclusions

XRM analysis was combined with deep learning workflow for the automatic detection of wall delamination defects of Cu liner TSVs in ASICs. Numerous XRM parameters were investigated to provide the two XRM measurement recipes. The workflow started with the short full device XRM measurements, enhanced by the algorithm from the deep learning-based defect detection (wall delamination), followed by detailed scans of TSVs of interest. The workflow presented a high output (70 TSVs) and could support both quality control and optimization of the complex fabrication process.

# One-step thermal gradient- and antisolvent-free crystallization of all-inorganic perovskites for highly efficient and thermally stable solar cells

Adapted from Byranvand, M. M., et al. 2022

All-inorganic perovskites of cesium lead halide, especially $CsPbI_2Br$, are promising photovoltaic materials with excellent thermal stability. The novel optimized one-step, solvent-free, thermal gradient method for the fabrication of $CsPbI_2Br$ films showed improvements in crystallization control, including nucleation and growth processes. These characteristics were compared to the $CsPbI_2Br$ films generated by the common method of thermal gradient (TG) annealing that ranged from 50 °C to 160 °C. Optical *in situ* characterization is used to monitor film formation during the steps and develop methods to enhance the evolving film attributes.

## Introduction

Ideal photovoltaic technology for industrialization not only needs high-power conversion efficiencies, but also long-term stability to moisture, oxygen exposure, and wide thermal fluctuations as well as an environmentally friendly fabrication process with minimal volatile organic components. Thermal gradient (TG) annealing (50 °C to 160 °C) is typically used for the crystallization of cesium lead iodide bromide ($CsPbI_2Br$) films. However, TG films have pinholes and nonuniform morphology. Several modifications have improved the film quality. This study provides a detailed spin-forced (SF) method that further improves the film quality, its thermal stability, and the fabrication process.

## Optimization of the one-step solvent-free thermal gradient method for generating $CsPbI_2Br$ films

Film formation with the SF method was monitored during the annealing and spin-coating (up to 200 s) and drying (additional 2,500 s) stages using *in situ* UV-vis spectroscopy. A longer spin-coating time alters the retention of DMSO in the film, changing the formation kinetics during annealing. The absorbance of the precursor solution declined during the initial seconds of spin-coating, which shifted the absorbance edge from 400 nm ± 10 nm to 430 ± 10 nm. It remained during the 200 s of the spin-coating phase. Byranvand and colleagues suggested that spin-coating and solvent extraction in the SF method homogenized the precursor film and did not induce significant nucleation or growth of the perovskite phase.

Absorbance of the SF-perovskite films generated by four different durations of spin-coating was compared using *in situ* UV-vis spectroscopy that revealed three phases (Fig. 1). A transition stage IIb induced with spin-coating times of 150 s and 200 s showed a slower shift of the absorbance edge than their stage II fast-initial shift (Figs. 1c,d vs 1a,b). The transition stage IIb may indicate a more homogeneous distribution of crystal growth, possibly due to a more controlled extraction of DMSO.

Different annealing temperatures (100 °C, 160 °C, and 200 °C) were investigated with the optimized precursor concentration (1.3 M) and spin-coating conditions (3,000 rpm, 150 s). The highest quality perovskite film was obtained using the 160 °C annealing temperature, as determined by the presence of stage IIb in the absorbance spectra with *in situ* UV-vis spectroscopy. X-ray diffraction (XRD) characterization revealed the crystallinity of the annealed $CsPbI_2Br$ films generated with different durations of spin-coating. The highest peak intensities detected by XRD occurred in the SF-150 samples.

## Characterization of SF-150 film

Byranvand and colleagues recorded top view and cross-sectional scanning electron microscopy (SEM) images to resolve the perovskite grain sizes and film morphologies of $CsPbI_2Br$ films fabricated by the optimized SF-150 method or the common TG method (Figs. 2a, b). The SF-150 fabricated $CsPbI_2Br$ film exhibited homogeneous morphology, uniform grain sizes, and reduced density of grain boundaries (Fig. 2a). The grain sizes uniformly expand to about 1 µm, which is significantly larger than the film thickness (≈450 nm). The cross-sectional SEM image of the SF-150 film confirmed a compact film morphology, which supports a consistent contact surface with the hole transport layer (HTL). Top view and cross-sectional SEM images of the SF-100 films show a higher density of GBs and much smaller grain sizes (Fig. 3a) than the SF-150 film (Fig. 2a). In comparable cross-sectional SEM images, SF-200 films show more nonuniformities (Fig. 3b) compared to SF-150 films (Fig. 2a).

In contrast, the conventional TG-fabricated $CsPbI_2Br$ film showed heterogeneous-sized crystallization with compact disordered morphology, varied thicknesses, small grain sizes of 200–500 nm, high density of grain boundaries, and numerous pinholes (Fig. 2b).

XRD characterization reveals the cubic $\alpha$-phase of both SF-150 and TG-fabricated $CsPbI_2Br$ films with no detectable $\delta$-phase (Fig. 2c). The diffraction peak intensities appeared almost twice as high in the SF-150 film than in the TG film.

Dynamics of charge carrier recombination were investigated with steady-state photoluminescence (SSPL) and time-resolved photoluminescence (TRPL) to further characterize and compare the quality of the perovskite

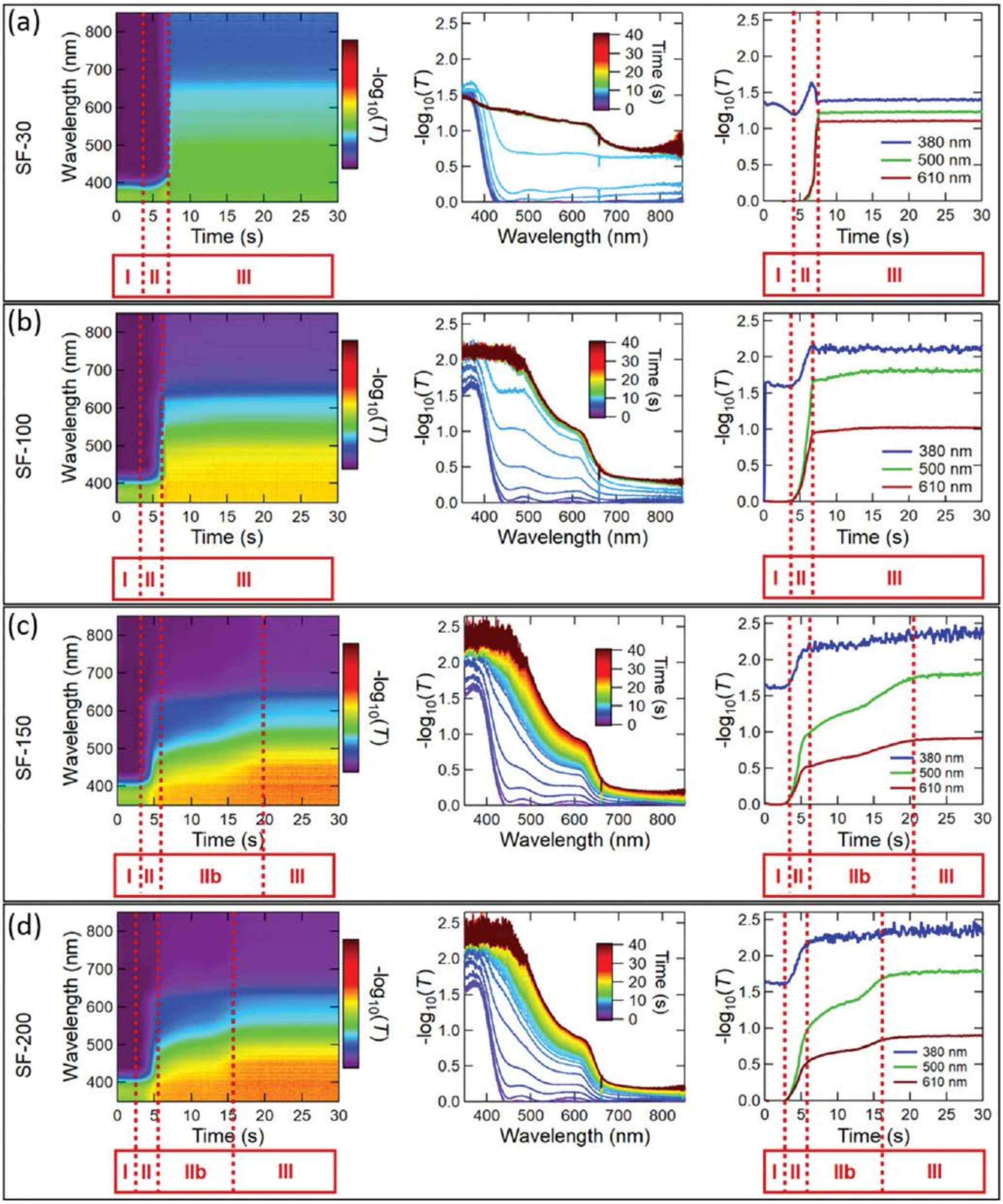

*Figure 1: Effect of different durations of spin-coating on the absorbance of SF-perovskite films: a) 30 s duration of spin-coating, SF-30; b) SF-100; c) SF-150; and d) SF-200. Absorbance was measured using* in situ *UV-vis spectroscopy. Left panel of each row shows an evolving contour plot of the film. Middle panel displays line scans at 10 s intervals versus wavelength. Right panel presents the quantity of three wavelengths (380 nm, 500 nm, 610 nm) as a function of time.*

films. The SF-150 film showed approximately 2-fold higher SSPL intensity compared to the TG film (Fig. 2d). Byranvand and colleagues suggested that the lower density of defects and higher SF-150 film quality greatly contributed to its decreased nonradiative recombination (Fig. 2d). TRPL provided quantitative data about the nonradiative surface and bulk recombination (Fig. 2e). The SF-150 film showed longer surface and bulk recombination lifetimes of 3.3 ns and 14.2 ns, respectively, compared to the TG film, with 1.9 ns and 8.2 ns (Fig. 2e), respectively.

Important parameters for photovoltaic efficiency were assessed on 30 each of SF-150- and TG-fabricated $CsPbI_2Br$ films on a bilayer of tin oxide (bi-$SnO_2$) as the electron transport layer (ETL) and Poly(3-hexylthiophene) (P3HT) as the HTL. Table 1 shows that the SF-150 films provided higher photovoltaic values than the TG films on the same matrix in all parameters.

Bi-$SnO_2$, two layers of tin oxide; ETL, electron transport layer; FF, fill factor; HTL, hole transport layer; $J_{sc}$, short circuit current; P3HT, poly(3-hexylthiophene; PCE, power conversion efficiency; Spiro, 2,2′,7,7′-Tetrakis(N,N′-dipmethoxyphenylamine)-9,9′-spirobifluorene; S-$SnO_2$, single layer of tin oxide; $V_{oc}$, open-circuit voltage.

One goal in photovoltaic research is the development of heat-stable photovoltaic cells. Comparison of the XRD patterns of six SF-150-fabricated films before and after heating to 300 °C for 1 h revealed minimal changes, with only the α phase evident. The six SF-150 PSCs also showed similar efficiency of power conversion. However, the XRD patterns of six TG-fabricated films after heating at 300 °C for 1 h showed a small δ phase peak. The power efficiency of the TG film had decreased by approximately 10% after heating at 300 °C for 1 h. Thus, the SF-150 films showed greater heat stability at 300 °C for 1 h than the TG-fabricated films.

## Summary

The novel optimized one-step solvent-free thermal gradient method for fabrication of $CsPbI_2Br$ films (SF-150) provided uniform films that showed improvements over the TG-fabricated films in crystallization control, lower density of defects and grain boundaries, larger grain sizes, more compact crystals, higher power conversion efficiency, and phase and thermal stability at 300 °C (1 h). Characterization of SF-150 fabricated films utilized SEM, XRD, and *in situ* UV-vis spectroscopy technology.

***Table 1:*** *Photovoltaic parameters obtained from the champion SF-and TG-PSCs fabricated with different ETLs and HTLs*

| Perovskite solar cells | PCE (%) | $J_{sc}$ (mA/cm$^2$) | FF (%) | $V_{oc}$ (V) |
|---|---|---|---|---|
| TG (S-$SnO_2$/Spiro) | 12.0 | 15.6 | 65.0 % | 1.18 |
| SF (S-$SnO_2$/Spiro) | 15.6 | 16.7 | 73.9 % | 1.26 |
| TG (bi-$SnO_2$/P3HT) | 14.2% | 16.0 | 74.2% | 1.19 |
| SF (bi-$SnO_2$/P3HT) | 17.0% | 16.6 | 80.5% | 1.27 |

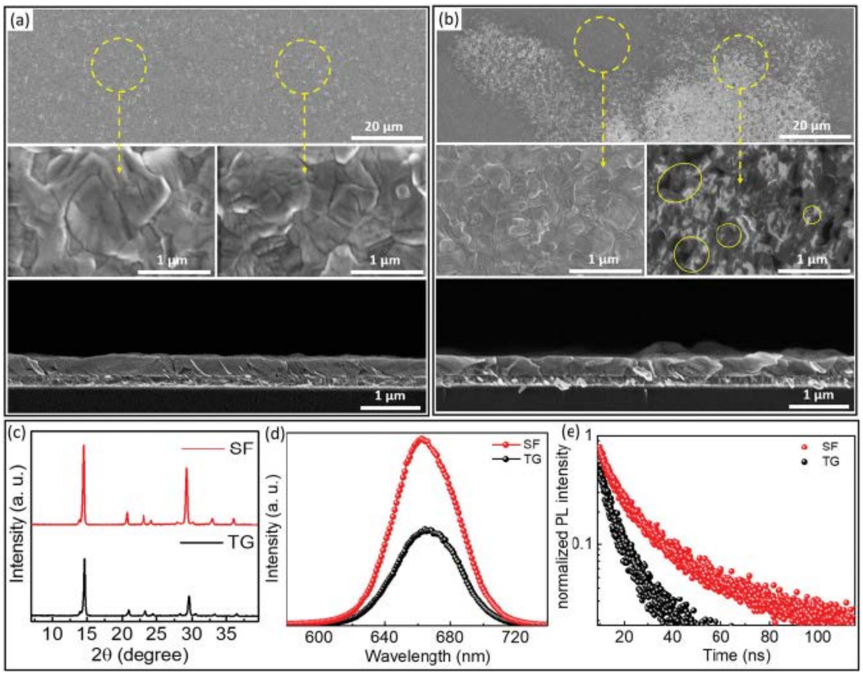

***Figure 2:*** *Characterization of SF-150 film and TG film. Top view and cross-sectional scanning electron microscope (SEM) images of (a) SF-150 film and (b) TG film. Characterization of both films by (c) X-ray diffraction (XRD), (d) steady-state photoluminescence (SSPL), and (e) time-resolved photoluminescence (TRPL).*

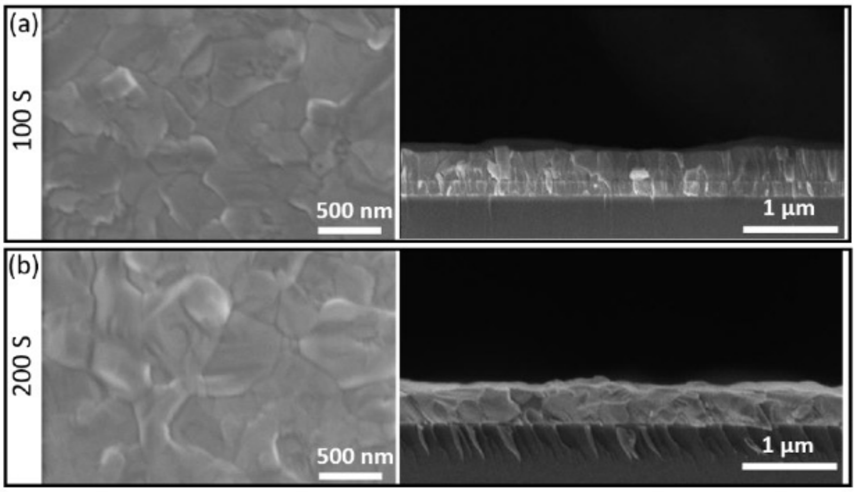

***Figure 3:*** *Top view and cross-sectional SEM images of (a) SF-100 and (b) SF-200.*

# Efficient combination of surface texturing and functional coating for very low secondary electron yield surfaces and rough nonevaporable getter films

Adapted from Himmerlich, M., et al. 2023

Particle accelerators, spacecraft, and satellites require materials with low secondary electron yield (SEY) or emission. SEY can be reduced by specific coatings. For example, the a-C/Ti (titanium doped amorphous carbon) coating reduced the SEY of the materials sufficiently in the Large Hadron Collider at CERN, and the super-proton-synchrotron for their function (SEY maximum of 2.18 $\delta_{max}$ reduced to 0.94 $\delta_{max}$). Additional coatings that potentially reduce current levels of SEY are sought to further suppress background noise and/or reduce distortion of the sought-after signal. SEY can also be reduced by surface roughening including deep trenches, grooves, and the production of nano- or micro-particles. The combination of nanostructured surface (versus flat) is being investigated with either a-C/Ti coating or relatively new coatings to further reduce backscattered, reflected, and secondary electrons (i.e., SEY). Scanning electron microscopy (SEM) was employed for surface characterization, and FIB-SEM (focused ion beam SEM) was used to prepare cross-sections and to determine film thickness.

## Introduction

Surfaces with SEY are sought for use in satellites, spacecraft, and particle accelerators. Electron collectors, ionization-based pressure gauges, and measurement of low electron currents in ultra-high vacuum (UHV) benefit from even lower SEY materials with reduced backscattered, reflected, and secondary electrons. Numerous material parameters affect SEY, including the presence of surface impurities or adsorbates, oxidation of surface metal, the chemical composition of the surface, and several modifications of the physical surface. SEY can be reduced by any of these treatments: thermal treatments, electron irradiation, thin film deposition such as coating with nonevaporable getter (NEG) film followed by its activation, machining of grooves or deep trenches, surface roughening, and several strategies that create a surface with micro- or nanostructures such as laser-induced surface structuring.

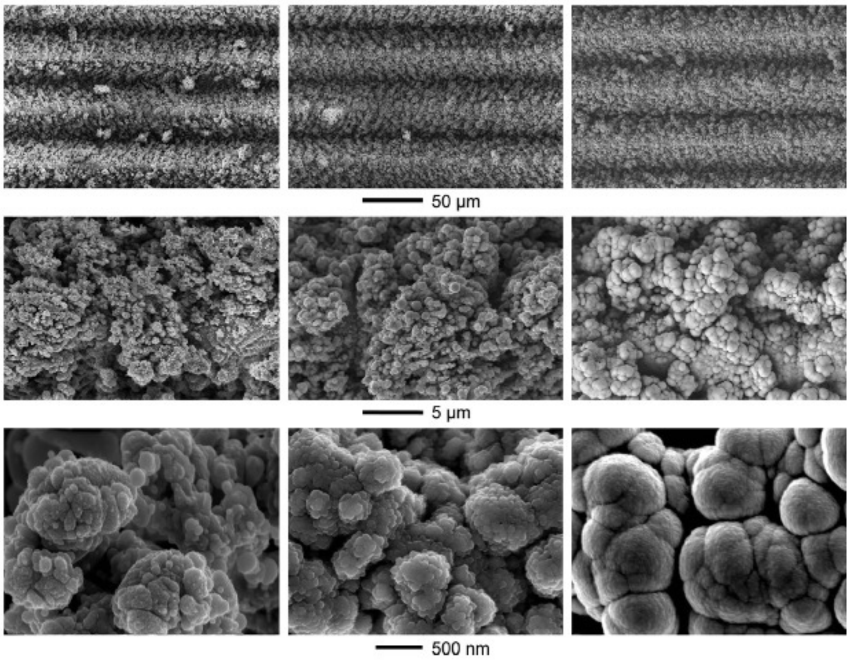

*Figure 1: Three different magnifications of top-view secondary electron micrographs of the copper platforms that received one of three treatments. Left panels: laser-treated copper surface; Center panels: laser-treated copper surface that received a-C/Ti coating; Right panels: laser-treated copper surface that received Ti–Zr–V coating NEG coating*

Three combinations, but not all combinations, of surface structuring and thin film deposition which change the surface composition, have been reported to reduce SEY. However, the contribution of each strategy was not fully elucidated. Here, the aims are to further reduce the SEY of the accelerator vacuum surface material by combining two strategies, a film coating of surface material and a roughening of the surface, and secondly to elucidate the contribution of each approach. The effect of two thin film coatings for accelerator vacuum technology on SEY on flat copper (Cu) surfaces were compared to their effects on laser-roughened Cu surfaces. The thickness of the films was at least 20-30 nm to ensure that all emitted secondary electrons arose only from the films.

## Characterization of the textured Cu surface and the film coatings

The textured Cu surface was induced by picosecond pulsed laser irradiation. Field emission scanning electron microscopy (SEM) was employed to characterize the specimen’s surface. A ZEISS Sigma system with Inlens secondary electron detector was utilized. Top-view SEM revealed a trench pattern covered by nanoparticles produced by the redeposition of the generated plasma plume (Fig. 1, left panels). The coating comprised titanium (Ti) with amorphous carbon layers (a-C/Ti) covered the nanostructures relatively evenly and maintained the initial topography (Fig. 1, center panels). Similarly, a titanium–zirconium–vanadium (Ti–Zr–V) nonevaporable getter (NEG) film also covered the nanostructures evenly on a microscale (500 nm) (Fig. 1, right panels). Both coatings induced smoothing of the initial topography as determined by structural and spectroscopic analysis at 50, 5, and 0.5 µm.

To determine the film thickness and the formed surface topography, a FIB system in dual beam configuration with scanning electron microscopy (ZEISS Crossbeam 540, gallium source) was used to prepare cross-sectional views. Figure 2 shows the film thickness due to physical vapor deposition of the top layers of the a-C/Ti- coating or the Ti–Zr–V coating in cross-sectional side views. The thickness of the a-C/Ti coating ranged from a few nanometers to 35 nm, which was thinner than the Ti–Zr–V coating (≤110 nm). In comparison, both the a-C/Ti film and Ti–Zr–V NEG films were thinner on the textured than the flat Cu surfaces (86 nm and 185 nm, respectively). Energy disperse X-ray spectroscopy (EDX) mapping was used to identify the different layers.

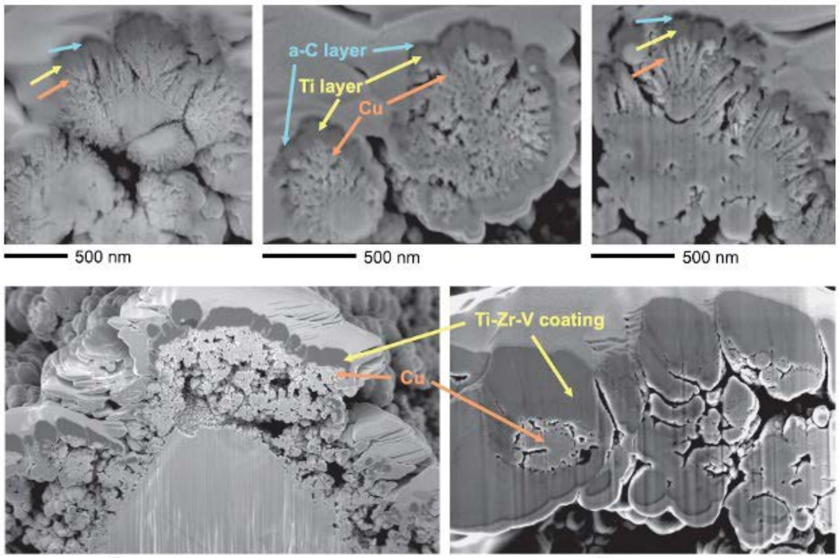

*Figure 2: Scanning electron microscopy cross-sectional images of the a-C/Ti coated Cu surface and Ti–Zr–V coated Cu surface. (Top row) Cross-sectional view of a-C/Ti coating on laser-treated Cu surface using focused ion beam (FIB) system; (Bottom row) Cross-sectional view of Ti–Zr–V coating on laser-treated Cu surface using FIB system.*

*Table 1: Effect of treatments on maximum SEY and its energy.*

| Sample | $\delta_{max}$ | Ep($\delta_{max}$) |
|---|---|---|
| Cu flat | 2.18 | 300 eV |
| Cu flat + a-C/Ti coating | 0.94 | 275 eV |
| Cu rough | 0.86 | 500 eV |
| Cu rough + a-C/Ti coating | 0.40 | 300 eV |
| Cu flat + Ti–Zr–V NEG coating | 2.01 | 300 eV |
| Cu flat + Ti–Zr–V NEG activated | 1.14 | 325 eV |
| Cu rough + Ti–Zr–V NEG coating | 0.92 | 400 eV |
| Cu rough + Ti–Zr–V NEG activated | 0.54 | 500 eV |

$\delta_{max}$, SEY maximum; Ep($\delta_{max}$), maximum energy of SEY maximum; NEG, nonevaporable getter films; SEY, secondary electron yield

Laser-roughening, a-C/Ti coating, and thermal activation of the Ti–Zr–V coating induce a significant reduction of SEY. Combining laser-roughening with either coating further reduced the SEY. Table 1 quantitatively shows the effects of the laser treatment, the coatings, and the combinations by providing the maximum SEY ($\delta_{max}$) and its energy Ep($\delta_{max}$) for each condition. The laser-treated Cu surface (rough) had a lower SEY maximum (0.86) than the flat Cu surface (2.18). The combination of the a-C/Ti coating on the laser-treated Cu surface further reduced the SEY maximum to 0.4 and the Ep($\delta_{max}$) to 300 eV. Similarly, the combination of activated Ti–Zr–V coating on laser-treated Cu surfaces further reduced the SEY maximum from 1.14 to 0.54.

## Conclusions

The top-view and cross-sectional electron micrographs clearly show that the dendritic fine structure of the particle's top side, which faces the ion flux during coating, is covered by the different deposited layers, while the particulate-induced surface topography is maintained. Therefore, the individual particle topography is changed after coating, leading to smoothing of the surface on the nanometer scale.

# Transparent fused nanowire electrodes by condensation coefficient modulation

Adapted from Lee, J., et al. 2022

Silver nanowire networks can be used as transparent electrodes for stretchable sensors, energy harvesting devices, and flexible optoelectronics with high performance. However, the complex fabrication of silver nanowires may limit their electrode utility and performance due to the high surface roughness and instability of the nanowire junctions. A new fabrication process uses silver vapor condensation onto electrospun nanofiber networks to produce junction-free, high-performance, flexible silver nanowire network electrodes. The advantages of this fabrication process are its simplicity (no mask, no dry metal or chemical etching step, nor mesh transfer step), scalability, sufficient low surface roughness, zero contact resistance between nanowires, and amenable to continuous roll-to-roll fabrication. These novel fabricated silver nanowires appear suitable for organic photovoltaic (OPV) devices and multiple other applications such as organic electronics. Scanning electron microscopy (SEM) enables the precise examination of the networks, for example, for junctions, gaps, aspect ratio, doping, mechanical strength, or heat stability.

## Introduction

Stretchable metal meshes and metal nano-network (NN) electrodes are used in many applications including organic photovoltaics (OPVs), wearable electronics, organic light-emitting devices, and transparent heaters. They are often fabricated from electrospun polymer nanofibers (NFs). Since contacts between nanowires are prone to overheating and oxidation, junction-free NNs are highly desirable. Since highly fluorinated organic compounds have a small condensation coefficient for Ag vapor, one or more of them may aid the fabrication of electrospun NNs with junction-free contacts. The utility of the Ag nano-networks fabricated with this simplified method is demonstrated in transparent, flexible heaters and transparent substrate electrodes, as examples of solution-processed OPVs.

## Fabrication

Authors report a new scalable approach for the fabrication of high-performance, junction-free transparent silver (Ag) nanowire network electrodes. This simplified fabrication process completely avoids the need for a complex metal nano-network transfer step or a metal etching step. These fabricated Ag electrodes have an average transparency of 90.8% across the wavelength range 400–800 nm and a sheet resistance of 6.3 Ω $sq^{-1}$.

As described in the literature, the spun polyvinylpyrrolidone (PVP) NFs do not fuse as shown by SEM images (Fig. 1a). Some parts are suspended above the substrate. SEM images show that the effects of desiccation with ethanol differ at the 10 min, 15 min,

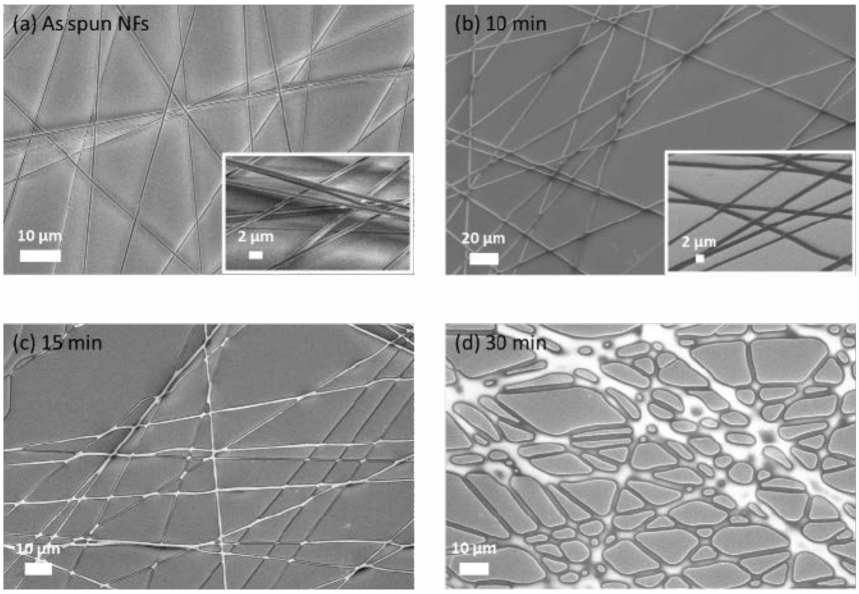

***Figure 1:** Optimization of PVP nanofiber (NF) fusion process. All images were collected using an SEM (ZEISS Gemini 500) with the PVP NFs supported on a silicon wafer to minimize charging. (a) as spun PVP nanofibers; (b-d) nanofibers kept in a desiccator with 1 mL ethanol at 800 mbar for indicated time: (b) 10 min; (c ) 15 min; and (d) 30 min. The insets are SEM images taken with some sample tilt.*

and 30 min time points, thereby supporting the use of SEM images to optimize the fabrication process (Figs. 1b-d).

### Transmittance of Ag nano-networks

The Ag nanowire networks fulfill the industrial requirements of 85% transmittance at 10-15 Ω as measured by a UV-Vis-NIR Spectrophotometer (LAMBDA 1050). The Ag NNs exhibited a direct current conductivity/optical conductivity ($\sigma_{DC}/\sigma_{Op}$) between 600 and 800.

### Mechanical and thermal stability

The methoxysilane additives (e.g., 3-aminopropyl trimethoxysilane (APTMS) and 3-mercaptopropyl trimethoxysilane (MPTMS)) on the PVP NFs described herein improved the mechanical and thermal stability of the Ag NN. SEM imaging revealed that the thermal stability of nanowire networks at 200 °C occurred only on methoxysilane-doped PVP NFs. In contrast, PVP NFs fabricated without methoxysilane additives and heated to 200 °C had formed disconnects and showed higher sheet resistance (Fig. 2b).

X-ray photoelectron spectroscopy (XPS) analysis provided evidence for cross-linking of the methoxysilane compounds (e.g., APTMS and MPTMS) which can form stable silicon (Si) Si–O–Si bonds in the nano-networks and increase the mechanical and thermal stability.

Mechanical strength can be monitored by SEM images. Representative SEM images indicate that the PVP nanofibers of the Ag nano-network that had been doped with APTMS:MPTMS and tested under 50% strain maintained many intact connections (Fig. 3 right panel). In comparison, the representative SEM image of the PVP nanofibers in the Ag nano-network fabricated without APTMS:MPTMS and tested under the smaller 30% strain revealed many junctions with a fracture and/or delamination (small red arrows) (Fig. 3 center panel).

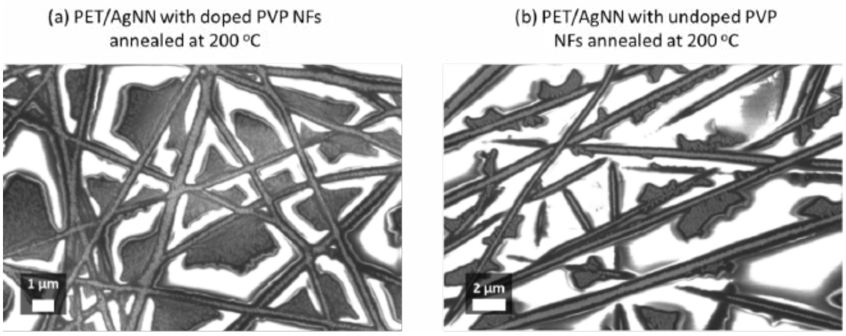

***Figure 2:*** *Thermal stability of Ag (100nm) nano-network electrodes on polyethylene terephthalate (PET) after annealing at 200 °C as illustrated by representative SEM images. (a) PVP nanofibers doped with APTMS:MPTMS; (b) PVP nanofibers without doping. In these tests, excess Ag condensed on exposed organofluorine regions was not removed before annealing. The elevated temperatures induced aggregation of Ag nanoparticles (red arrows). SEM images were obtained using ZEISS Gemini 500. APTMS, 3-aminopropyl trimethoxysilane; MPTMS, 3-mercaptopropyl trimethoxysilane.*

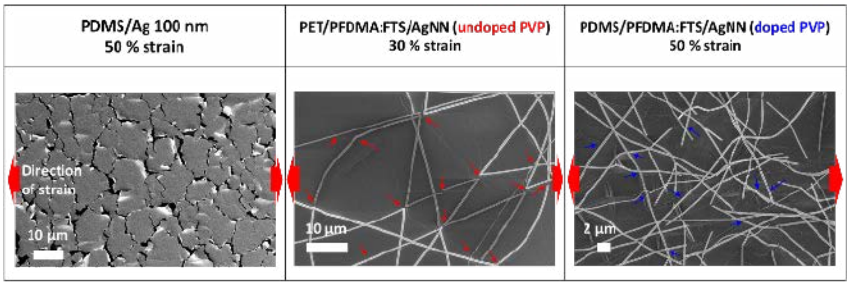

***Figure 3:*** *SEM images of stretching test results on an Ag thin film (left panel), Ag nano-network without APTMS:MPTMS doping of the PVP nanofibers (center panel), and Ag nano-network with APTMS:MPTMS doped PVP nanofibers (right panel). Small red arrows indicate fracture and/or delamination. Small blue arrows indicate intact connections. APTMS, 3-aminopropyl trimethoxysilane; MPTMS, 3-mercaptopropyl trimethoxysilane; PVP, polyvinylpyrrolidone (nanowires).*

### Transparent heaters and photovoltaic solar cells

The fused Ti–Zr–V nano-networks on PET substrates were investigated as flexible transparent heaters in comparison to the indium tin oxide (ITO)-doped nanowires on polyethylene naphthalate (PEN) flexible substrates. An infrared thermal imaging camera (FLIR i5) was used to measure the temperatures. The Ag NN heated up at voltages lower than those required to heat ITO nanowires. Importantly, these voltages for the Ag nanowires are lower than those typically used for window heaters in automobiles. In comparison to ITO temperature changes, the temperature of the Ag NNs stabilizes more quickly and its heat distribution is uniform at 5V regardless of bending. Conformal poly(3,4-ethylenedioxyxythiophene) (PEDOT):polystyrene sulfonate (PSS) coating of the Si wafer/PFDMA:FTS/Ag nano-network/PEDOT:PSS was demonstrated with SEM images. The Ag nanowire networks on PET substrates have narrow diameters and a flattened fused morphology. The consistent high-quality Ag NN fabricated by this method suggests suitability for OPV devices. These transparent PET/Ag substrate electrodes showed dose-dependent enhancement of current-voltage density in simulated sunlight, compared to dark conditions, further demonstrating their potential as transparent electrodes in OPV devices.

### Summary

This novel fabrication method for Ag NNs reduces the complexity of manufacturing, roughness of electrode surface, and junction disconnects. Additional advantages include simplicity of fabrication, zero contact resistance between nanowires, amenable to roll-to-roll fabrication and compatibility with producing a photoactive layer of 100 nm thickness.

# Durable, highly sensitive conductive elastomeric nanocomposite films containing various graphene nanoplatelets and their derivatives

Adapted from Meng, Q., et al. 2022

Flexible strain sensors are used in human motion monitoring, biomedicine, structural monitoring, human-machine interaction, and intelligent robotics. They can convert signals of external mechanical deformation to electrical signals. Improvements to flexible multifunctional polymer matrices are sought since uneven dispersion of nano-fillers can hinder their performance. This study investigated and reported several methods of preparing graphene nanosheets that improve their dispersion as nano fillers and the compatibility of nanosheets in a polydimethylsiloxane (PDMS) matrix. Their two types of modified graphene (MGE and BMGE) are more evenly dispersed in the PDMS matrix than unmodified graphene. The MGE/PDMS composite film exhibits improved functional characteristics: Electrical conductivity, high sensitivity, broad sensing range, a response time of 0.12 s, and reliable cycle repeatability (>10,000).

## Introduction

The advantages of flexible strain sensors include high flexibility, longevity, lightweight, and good compatibility. The indicators of the sensing performance of flexible strain sensors include linearity, sensitivity, response time, sensing range, and repeatability. Highly stretchable and flexible composite films are usually an integral component of flexible strain sensors. Numerous strategies are being investigated for fabricating the optimal composite film with the desired characteristics. Ensuring even dispersion of the components (e.g., conductive nanomaterials with flexible substrate) is a critical challenge during fabrication. Although graphene has a large surface area, excellent stability, and superb conductivity, several modifications such as ball milling and silane coupling agent 3-aminopropyltriethoxysilane (APTES) can improve its compatibility and dispersion in polymeric substrates. In this study, the morphology, thickness, and dispersion of three types of graphene fillers and their co-blending in composite films were compared. The mechanical and sensing properties improved in the composite films which are attributed to better dispersion.

## Experimental section

Samples of naïve graphene nanoplatelets (GNP) were ball-milled for 15 h (BGE-15 h), and some were modified with APTES: MGE is APTES-modified BGE-15 h. Ball-milled graphene powder for 9 h is called BGE-9 h and BMGE is APTES-modified BGE-9 h. Composite films used the polydimethylsiloxane (PDMS) matrix.

## Characterization of graphene nanoplatelets, ball-milled graphene, and ball-milled modified graphene

X-ray diffractometer (XRD) analysis of treated and untreated graphene revealed a significant decrease in peak intensity of BGE-15 h and MGE compared to GNP, which corresponds to the opening of graphene lamellae, increased sheet spacing, and a decrease in crystal integrity. The Raman spectra showed the D, G, and 3D peaks in all samples. The small D peak of GNP corresponds with its good degree of order. The higher D peak intensities of MGE, BGE-15 h, and BMGE samples correspond with higher levels of disordered carbon content and defects after ball milling. The Fourier transform infrared spectrometer (FTIR) spectra of MGE and BGE-15 h reveal different peaks for the stretching vibration of C–O–C and bending vibration of C–OH. APTES treatment also induced different absorption peaks that correspond to Si–O–Si and Si–O bonds in both samples. The thermogravimeter analyzer (TGA) curves reveal significant improvement in the thermal properties of BGE-15 h, MGE, and BMGE after APTES modification. Atomic force microscopy (AFM) reveals the thickness of GNP, BMGE, and MGE as 3.86 ± 0.12 nm, 4.91 ± 0.11 nm, and 1.71 ± 0.17 nm, respectively. The thinner nanofiller suggests the composite films have more dispersed graphene sheets.

## Mechanical property

Composite films with higher flexibility as well as compressive and tensile strength are advantageous in practical applications. The mechanical properties of the GNP/PDMS, MGE/PDMS, and BMGE/PDMS composite films were measured by the tensile strength machine and tensile sensor. The tensile strength is dependent on the amount of filler. The calculated elongation at break and Young's modulus revealed that the BMGE/PDMS composite film had the highest tensile strength of the group.

## Electrical conductivity

The film conductivities of GNP/PDMS, MGE/PDMS, and BMGE/PDMS compos-

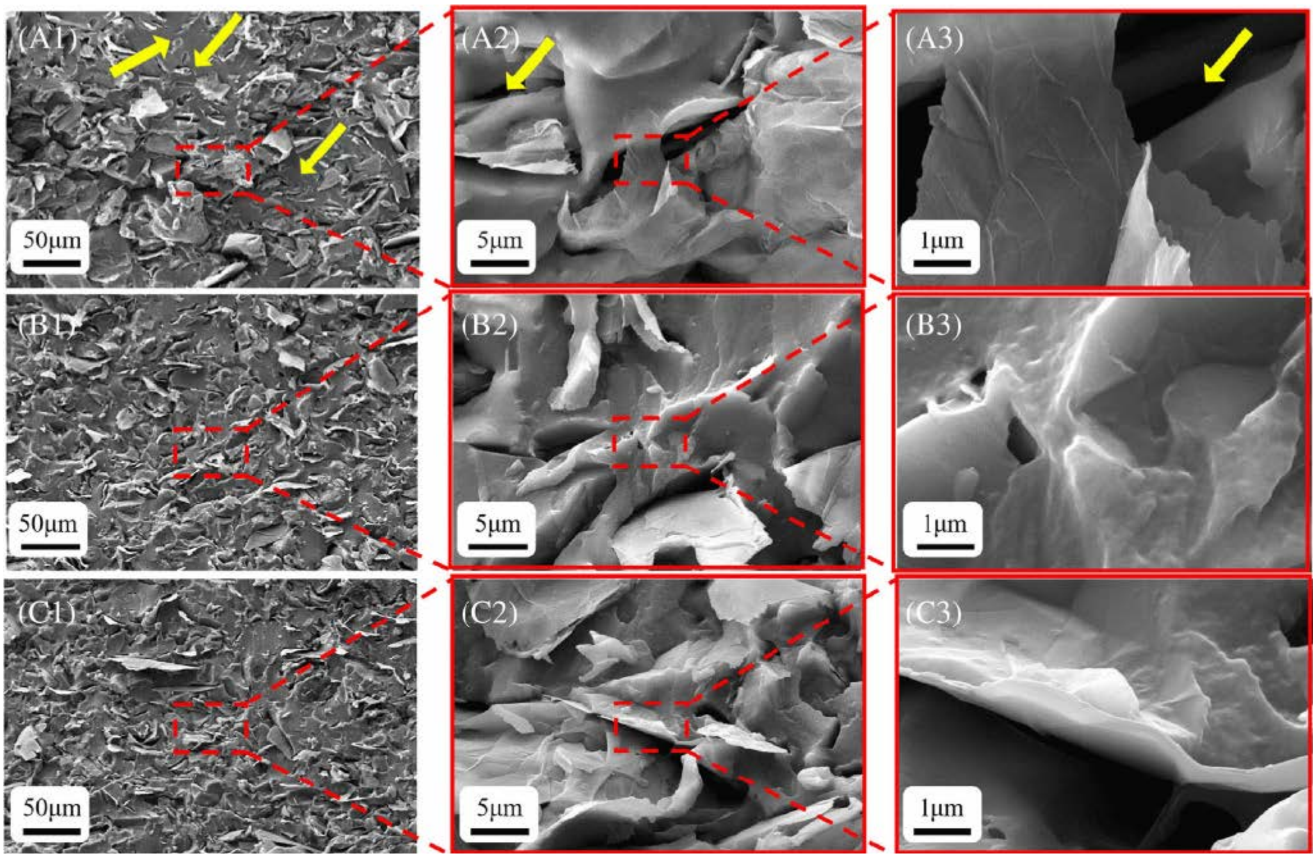

***Figure 1:*** *SEM cross-sectional images at three magnifications of three composite films: (A) GNP/PDMS composite film; (B) MGE/PDMS composite film; (C) BMGE/PDMS composite film.*

ite films were measured by using an insulation resistance meter and a film thermoelectric parameter testing system. The conductivity is poor when a filler is less than 1.5% of the volume of the composite film, but increases sharply as the volume of filler increases from 1.5% to 2.8%. The conductivity grows slowly when the volume of filler is above 2.8% in the composite film. The percolation thresholds of GNP/PDMS, MGE/PDMS, and BMGE/PDMS composite films are 2.27%, 2.31%, and 2.66%, respectively. Meng and colleagues chose to investigate the remaining properties of these types of composite films fabricated with a 3% filler.

## Film morphology analysis

Field emission scanning electron microscope (SEM) images of GNP/PDMS, MGE/PDMS, and BMGE/PDMS composite films revealed that they had various levels of dispersion of their graphene components (Fig. 1). Figure 1A shows a relatively flat region with few GNPs in the area and several voids (yellow arrows) which provide examples of nonuniform dispersion of GNP in the GNP/PDMS composite film. In comparison, folded regions occur throughout the cross-section of MGE and the MGE/PDMS film has fewer gaps than GNP/PDMS films (Fig. 1B). The SEM images and thinner MGE support a higher number of MGE sheets in the composite film, confirming a more uniform dispersion of MGE (Fig. 1B). The structures of the BMGE/PDMS film have fewer wrinkles and more gaps than the MGE/PDMS film, likely due to fewer sheets of the thicker BMGE in the film. The cross-sectional morphologies of the films were observed using a Sigma 300 SEM from ZEISS.

## Sensing performance

An important property of sensors is sensitivity, which is expressed as a gauge factor (GF). During testing, both ends of the composite film are fixed to a tensile machine jig which provides a constant tensile speed. GNP/PDMS, MGE/PDMS, and BMGE/PDMS composite films exhibited sensing ranges of 40%, 48%, and 57%, respectively. The GF increases with higher strain. The results revealed that BMGE/PDMS composite films were less sensitive than MGE/PDMS films. BMGE/PDMS films did not meet the sensitivity requirements of numerous devices.

The resistances of the composite films showed good flexibility, even with a bending angle of 180° which supports their potential to monitor bending deformation. The changes in resistance for GNP/PDMS, MGE/PDMS, and BMGE/PDMS composite films are approx. 5 times, 7.5 times, and 4 times, respectively.

The response time indicates the time that a sensor takes after being stretched to change its resistance. The response times of GNP/PDMS, MGE/PDMS, and BMGE/PDMS composite films are 0.15, 0.12, and

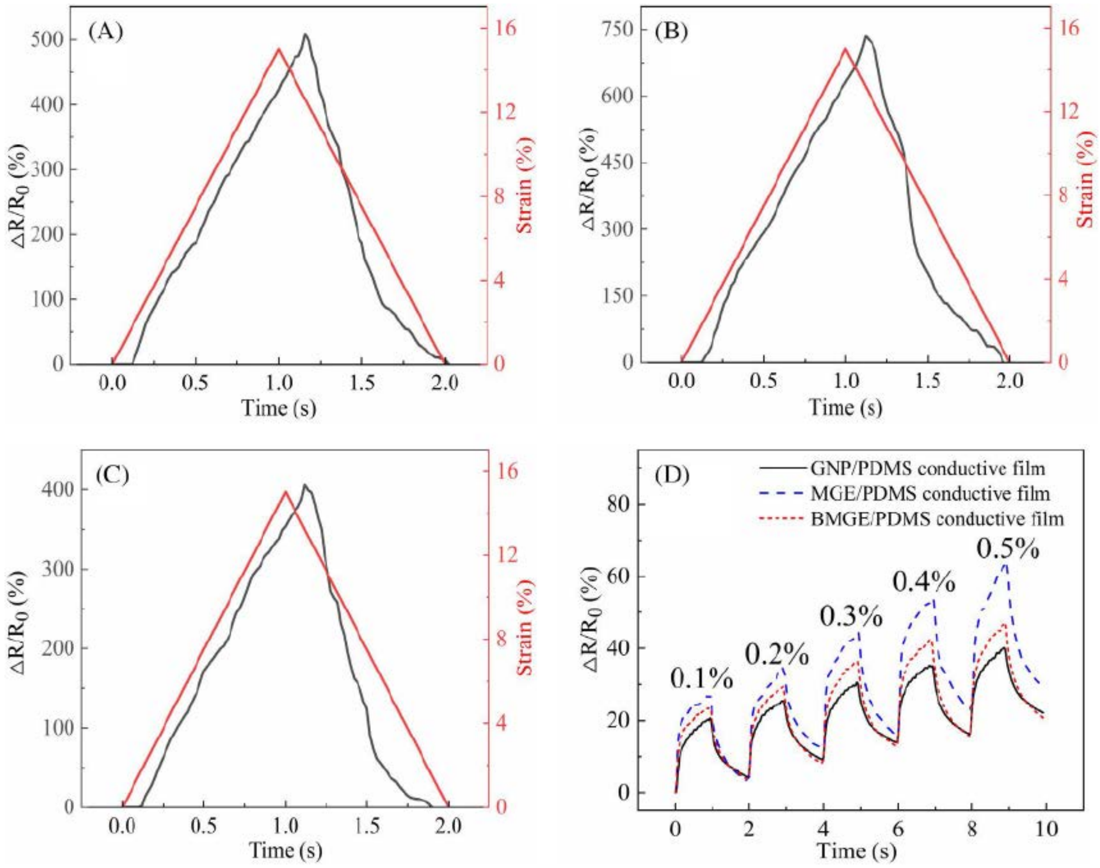

***Figure 2:*** *Response time and relative resistance properties of three composite films. The response times of (A) GNP/PDMS; (B) MGE/PDMS; (C) BMGE/PDMS. (D) The relative resistance variation step tensile strains of the three composite films.*

0.12 seconds, respectively (Fig. 2A, B, C). As shown in Figure 2D, the composite films can detect tensile deformation ranging from 0.1% to 0.5%, i.e., minor changes. In assessing repeatability, the MGE/PDMS and BMGE/PDMS films were more stable in their resistance change ranges than GNP/PDMS films, even after 3,000 to 10,000 cycle load-unload tests.

## Conclusion

A comparison of three distinct graphene filler preparations in composite films (GNP/PDMS, MGE/PDMS, and BMGE/PDMS) indicated that the size, thickness, and dispersion of graphene filler sheets affect the mechanical and electrical properties. BMGE/PDMS films had the lowest sensitivity but are most flexible in mechanical properties. MGE/PDMS films had the highest sensitivity which suggests their potential for future monitoring applications.

# Exploring nanoscience: Innovations, challenges, and research insights

## An interview with Silke Christiansen, a nanoscience expert, on inspiring careers and cutting-edge research

In this captivating interview, we delve into the world of nanoscience with a prominent expert in the field, Prof. Silke Christiansen. Discover the motivations behind a career in nanoscience, the essence of nanoscience explained for non-specialists, and gain insights into groundbreaking research in X-ray microscopy and deep learning object detection for automatic defect location on liner-through-silicon-vias. Uncover the challenges faced in this interdisciplinary domain and the strategies employed to overcome them, as we explore the frontiers of nanoscience and its profound impact on various industries.

**What inspired you to pursue a career in nanoscience?**

***S. Christiansen:*** I pursued a degree in Materials Science at Friedrich Alexander University in Erlangen, Germany, as it provided a diverse combination of physics, chemistry, and economics without requiring me to specialize right away. Over time, the field of Materials Science has evolved into Nanoscience, adding even more excitement to the discipline. The incorporation of biomaterials and biological tissues into the field has further enhanced its appeal. Moreover, the course curriculum and job opportunities not only focus on materials but also encompass various components, technical systems, devices, and applications.

**How would you explain nanoscience to someone who is not familiar with the field?**

***S. Christiansen:*** Nanoscience is a dimension specification. Nanomaterials contain structure sizes ranging from a few to several tens of $10^{-9}$ meters. The properties of such nanomaterials differ from those of their bulk counterparts. The large surface area of nanomaterials alone enables a material and component design that would not be possible with bulk material in a similar form. Nanomaterials open up completely new design freedoms for technical systems built from them.

**Could you tell us about your current research at the Fraunhofer Institute for Ceramic Materials and Systems and at the Institute for Nanotechnology and Correlative Microscopy in Forchheim, Germany?**

***S. Christiansen:*** I coordinate a research department that essentially relies on a world-class analytics lab with microscopes, spectrometers, and computed tomography machines. With these, we perform cross-scale analyses using focused electron beams, ion beams, probes, and focused laser light to assess of physical properties of materials and devices such as electrical, optical, structural, mechanical, compositional, chemical, and topographic properties in 2D and 3D. All is connected, so data can be analyzed using software powered by machine learning to help us create a digital twin and intelligently and efficiently drive materials and device optimization.

We follow the very same approach that includes a thorough focus on efficient sample preparation for various areas of research and innovation including (i) energy materials and devices such as batteries, fuel cells, and solar cells, (ii) sensing devices such as electronic nose devices, (iii) semiconductors in micro- and nano-electronic devices as well as light-emitting devices, large area devices such as displays and solar cells, and power electronic devices, (iv) biotechnology devices such as implants, dental fillings, health monitoring devices and many more.

By emphasizing analytics, imaging, and data-driven business models, our tools have the versatility to contribute to a variety of innovation fields and address many different application areas. The group of national and international cooperation partners and business customers is also constantly expanding, which brings with it constant inspiration.

**How do you approach designing experiments in your research, and what are some of the key considerations you take into account?**

***S. Christiansen:*** The design of experiments depends heavily on the fields of application and research questions. If a customer brings us an air-sensitive battery material for analysis, we have to perform all our analysis in an inert environment and often even have to rely on liquid nitrogen cooling during preparation and imaging. Then, there are other materials, e.g., complex building material composites that do not have any sensitivities but components may catch fire, or other materials that may be toxic and therefore require precise handling. Other materials such as biological tissues require handling in biological safety laboratories and appropriate sample preparation and disposal. We are prepared for all challenges and have respective sample preparation tooling, preparation labs, and analytics.

**What are some of the biggest challenges you face in your current research, and how are you working to overcome them?**

***S. Christiansen:*** The great interdisciplinarity of our customers and the associated

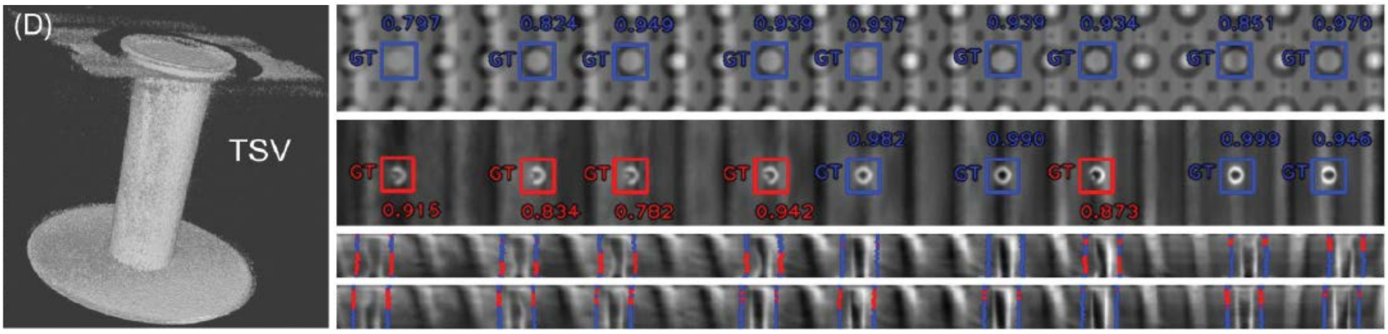

research targets and samples are challenging. We need to accumulate a substantial amount of expertise and establish a competent and collaborative interdisciplinary team to handle that. It requires a lot of training, and we have to work to develop and retain our experts. The possibilities of competitive pay currently show us the limits of keeping the best minds on the team. It is our strategy to create an inspiring working environment with a world-class laboratory that invites people to conduct bleeding-edge research. This inspires those critical minds that we urgently need.

**Could you describe your research on X-ray microscopy and deep learning object detection for automatic defect location on liner-through-silicon-vias (TSVs) in more detail?**

***S. Christiansen:*** The published research was triggered by real industrial needs to understand and optimize defect-free processing of silicon chips, specifically those with large through-silicon-vias (TSVs) with metallization layers, in these high aspect ratios via structures.

Microscopic X-ray tomography plays a significant role in semiconductor device research and microelectronics by enabling non-destructive three-dimensional imaging and analysis of internal structures and features, such as the in-via metallization layers. X-ray microscopy (XRM) provides valuable insights into the composition, morphology, and packaging of semiconductor devices, helping researchers and engineers understand their performance, reliability, and failure mechanisms. In the particular case of this study, the XRM combined with automated image analysis with the help of machine (deep) learning, was used for swift and reliable failure analysis based on fast scans for which proper training was carried out based on standardized medium magnification scans assisted by high-resolution XRM scans, which are, of course, substantially slower.

In our case, the failure analysis workflow based on XRM tomography data was used to study metallization delamination, as well as voids and related issues within the semiconductor devices, without destroying the device. By visualizing these defects in three dimensions, researchers can identify the root causes of failures and optimize the design and manufacturing processes accordingly.

**Why is the development of evaluated scan recipes or best practices for XRM parameter settings important for the study of TSVs?**

***S. Christiansen:*** Particularly for studies in industry rather than academic environments, the price of measurement is crucial for determining the appropriate characterization technique, ensuring quality maintenance, and guiding the development of designs or processing procedures. In academic research, we might strive for the best dataset, with the highest resolution to demonstrate a feature for publication. However, this is different when industrial at-line analytics is involved. Here, the measurement time on a machine plays a role in the calculation of procedural costs. As a result, automation is receiving significant attention within the industry. The automated assessment of the defect population using machine learning algorithms is the preferred procedure when it comes to saving time and costs. In the same context, the training of a blurred fast scan with high-resolution data to use the fast scan data, in the long run, is as well a procedure of industrial relevance. In the present paper, we demonstrate both approaches and, with varying settings and parameters, we can have low- and high-magnification, short scan and long-time scanning procedures, respectively.

**How did you select the measurement setups and parameters used in your study, and what were some of the key considerations you took into account?**
**Christiansen:** We chose parameters optimized for the best contrast and resolution while maintaining minimum time on the machine. We used medium-resolution scans with high statistical significance to train for automated, machine learning-based assessment. Furthermore, our high-resolution scan recipes proved the presence of defects observed at a lower resolution and led to a better understanding of artifacts. In summary, we used the large volume scans at lower resolution to familiarize ourselves with a larger volume and the ‘resolution at a distance’ option to zoom in and assess in more detail those TSVs that showed, for example, bad electrical behavior.

**Could you explain the RetinaNet-based object detection method you used in your research and how it achieves a high average precision for automated defect analysis?**

***S. Christiansen:*** A RetinaNet is a good choice for automated feature detection in images, when only a limited and imbalanced dataset is available, which are the conditions we have here. Object recognition networks like the RetinaNet mimic expert behavior by detecting and classifying objects while assessing the reliability of their detection using scores, thereby offering a good trade-off between accuracy and speed. The RetinaNet architecture consists of a single network that uses a backbone as a feature extractor and multi-scale features that are then generated using a feature pyramid network (FPN). The net uses low-resolution but semantically strong features at the down-sampled layers and high-resolution but semantically weak features at the layers that are closer to the original image size. Each layer of the FPN in this process is used for classification and regression via subnetworks in order to provide predictions on different scales. The regression network is used to determine the coordinates for the bounding box containing the target object. To address the class imbalance, the FocalLoss algorithm was employed in this study, which dynamically down-weights the contribution of easily and well-classified samples and lets the model focus on the difficult cases.

**How do you see the combination of XRM and deep learning object detection being used for failure analysis, quality control, or process optimization in R&D environments?**

***S. Christiansen:*** I see this combination as a must for all research labs in the future, not only in academia but also in industrial environments. The XRM is needed to carry out a non-destructive, large-volume assessment of any sample. Based on that, critical areas are identified for deeper, high-resolution studies. These can be carried out using the 'resolution-at-a-distance' (RaaD) technique of the Versa 620 XRM. But a problem arises because RaaD usually requires long-lasting and costly scans. Using only a few of them to train an algorithm that allows extraction of features like defects, impurities, processing instabilities, etc., from low-cost, low-resolution scans is the way to go when time on a machine and costs play a decisive role. I see tremendous opportunities to use this essentially non-destructive combination of characterization and data processing to advance process optimization in device manufacturing of various kinds.

**What do you think are some of the potential limitations or challenges of using this approach, and how might they be addressed in future research?**

***S. Christiansen:*** The limitation is for now that experts need to be involved to carry out this image processing/data assessment and algorithmic work. Easy-to-use software tools for all those that just want to use data from a microscope rather than work with it are needed. I see this as a chance for high-tech SMEs that can provide that software or services. Another aspect is the identification and distinction of defects and tomography artifacts in XRM by the experts, which are especially present in semiconductors with an inhomogeneous distribution of Z materials, e.g., silicon and high Z solder materials.

**Are there any other applications of X-ray microscopy and deep learning object detection that you're particularly excited about or interested in exploring in the future?**

***S. Christiansen:*** Yes, tons of those. I see the XRM at the beginning of each analytical 'food chain', which can be followed, for example, by in-depth studies with SEM-based analytics or molecular fingerprinting using optical spectroscopies. Before these in-depth, multi-modal analytical studies start, the XRM volume analysis can be used to develop a statistical assessment of how many defects of a type are present before an individual defect is further assessed.

To make this workflow fully practical and usable, there must be a step in between that permits an easy cut out of the area of interest, i.e., in our case the area with the defect for further analytics, e.g., with SEM-based analytics or spectroscopies. Cutting out might be doable with a focused ion beam (FIB) in a FIB-SEM or with an ultra-short-pulse laser that can be directed to the region of interest (ROI) obtained from the XRM volume scan with the additional help of marker layouts and software.

Cases where this workflow could be the most suitable range from semiconductor technology (e.g., systems-in-package, semiconductor devices from the area of micro-/nano-/power- and large-area electronics, etc.) to battery research, fuel-cell, and electrolysis devices, micro-fluidics chips, sensor systems (e.g., for environmental sensing), materials from the bio-medical field such as implants, artificial skin, filter systems and many more. The end of imagination limits the potential use cases you can think of.

## Silke Christiansen

**Silke Christiansen has been appointed full professor since 2013 at the Free University – Berlin in the physics department and is managing a research department for 'Correlative Microscopy and Materials Data' at the Fraunhofer Institute for Ceramics materials and systems in Forchheim, Germany. She received several awards including the MRS student award, a research fellowship award by the Bayerische Forschungsstiftung for a research stay at Columbia University, NY, USA, and a Feodor Lynen Fellowship awarded by the Alexander von Humboldt Foundation to carry out research in silicon technology at TJ Watson Research Center of IBM, Yorktown Heights, NY, USA. Moreover, she is a distinguished honorary professor at the Material Science Dept., Chungbuk University in Korea.**

**She has significant experience in the field of nanomaterials, in particular energy materials and context microscopy and spectroscopy, biomedical sensing, biotechnology, and opto- as well as large-area electronics. She advances materials based on correlated microscopies and spectroscopies for which she operates a labs@location unit with ZEISS Research Microscopy Solutions. She has more than 380 peer-reviewed publications, 12 patents/applications, 200 invited seminars, 120 invited keynote and plenary talks at international conferences, and ~ 15,400 citations and an h-index of 64.**

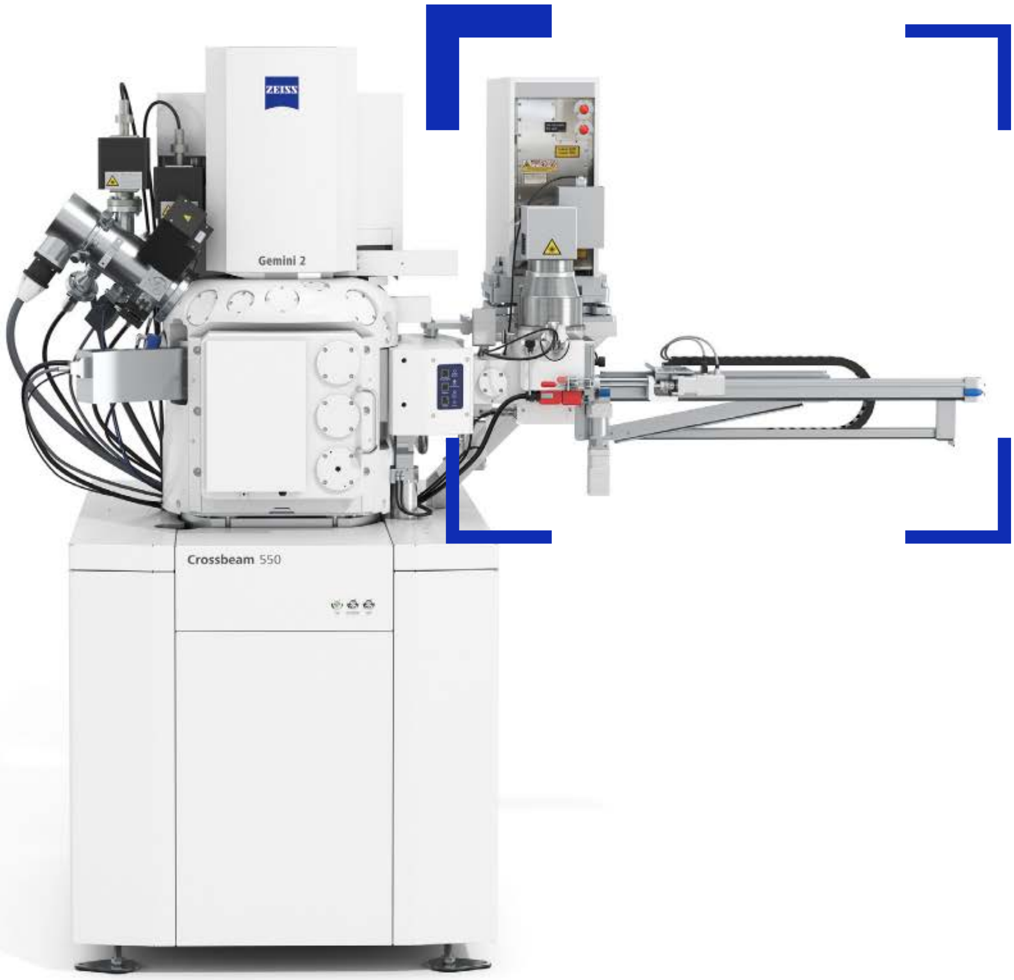
ZEISS
Gemini 2
Crossbeam 550

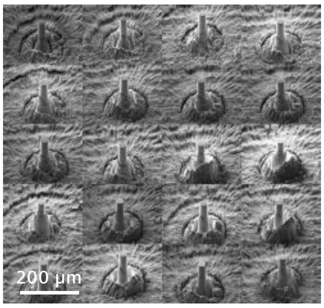
200 µm